First hot corino detected around an isolated intermediate-mass protostar: Cep E-mm

J. Ospina-Zamudio, B. Lefloch, C. Ceccarelli, C. Kahane, C. Favre, A. López-Sepulcre, M. Montarges

A&A 618, A145 (2018)
https://doi.org/10.1051/0004-6361/201832857

Astronomy & Astrophysics

First hot corino detected around an isolated intermediate-mass protostar: Cep E-mm

J. Ospina-Zamudio[1], B. Lefloch[1], C. Ceccarelli[1], C. Kahane[1], C. Favre[2], A. López-Sepulcre[1,3], and M. Montarges[4]

[1] Univ. Grenoble Alpes, CNRS, IPAG, 38000 Grenoble, France
e-mail: juan-david.ospina-zamudio@univ-grenoble-alpes.fr
[2] INAF, Osservatorio Astrofisico di Arcetri, Largo E. Fermi 5, 50125 Firenze, Italy
[3] IRAM, 300 rue de la Piscine, 38406 Saint-Martin-d'Hères, France
[4] Institute of Astronomy, KU Leuven, Celestijnenlaan 200D B2401, 3001 Leuven, Belgium

Received 19 February 2018 / Accepted 22 July 2018

ABSTRACT

Context. Intermediate-mass (IM) protostars provide a bridge between the low- and high-mass protostars. Despite their relevance, little is known about their chemical diversity.
Aims. We want to investigate the molecular richness towards the envelope of I-M protostars and to compare their properties with those of low- and high-mass sources.
Methods. We have selected the isolated IM Class 0 protostar Cep E-mm to carry out an unbiased molecular survey with the IRAM 30 m telescope between 72 and 350 GHz with an angular resolution lying in the range 7–34″. Our goal is to obtain a census of the chemical content of the protostellar envelope. These data were complemented with NOEMA observations of the spectral bands 85.9–89.6 GHz and 216.8–220.4 GHz at angular resolutions of 2.3″ and 1.4″, respectively.
Results. The 30 m spectra show bright emission of O- and N-bearing complex organic molecules (COMs): CH_3OH and its rare isotopologues CH_2DOH and $^{13}CH_3OH$, CH_3CHO, CH_3OCH_3, CH_3COCH_3, HCOOH, $HCOOCH_3$, H_2CCO, NH_2CHO, CH_3CN, C_2H_3CN, C_2H_5CN, HNCO and H_2CO. We identify up to three components in the spectral signature of COMs: an extremely broad line (eBL) component associated with the outflowing gas ($FWHM > 7$ km s^{-1}), a narrow line (NL) component ($FWHM < 3$ km s^{-1}) associated with the cold envelope, and a broad line (BL) component ($FWHM \simeq 5.5$ km s^{-1}) which traces the signature of a hot corino. The eBL and NL components are detected only in molecular transitions of low excitation and dominate the emission of CH_3OH. The BL component is detected in highly excited gas ($E_{up} > 100$ K). The NOEMA observations reveal Cep E-mm as a binary protostellar system, whose components, Cep E-A and Cep E-B, are separated by ≈1.7″. Cep E-A dominates the core continuum emission and powers the long-studied, well-known, high-velocity jet associated with HH377. The lower flux source Cep E-B powers another high-velocity molecular jet, reaching velocities of ≈80 km s^{-1}, which propagates in a direction close to perpendicular with respect to the Cep E-A jet. Our interferometric maps show that the emission of COMs arises from a region of ≈0.7″ size around Cep E-A, and corresponds to the BL component detected with the IRAM 30 m telescope. On the contrary, no COM emission is detected towards Cep E-B. We have determined the rotational temperature (T_{rot}) and the molecular gas column densities from a simple population diagram analysis or assuming a given excitation temperature. Rotational temperatures of COMs emission were found to lie in the range 20–40 K with column densities ranging from a few times 10^{15} cm^{-2} for O-bearing species, down to a few times 10^{14} cm^{-2} for N-bearing species. Molecular abundances are similar to those measured towards other low- and intermediate-mass protostars. Ketene (H_2CCO) appears as an exception, as it is found significantly more abundant towards Cep E-A. High-mass hot cores are significantly less abundant in methanol and N-bearing species are more abundant by two to three orders of magnitude.
Conclusions. Cep E-mm reveals itself as a binary protostellar system with a strong chemical differentiation between both cores. Only the brightest component of the binary is associated with a hot corino. Its properties are similar to those of low-mass hot corinos.

Key words. astrochemistry – stars: formation

1. Introduction

The chemical composition of protostellar envelopes and their properties along the evolutionary stage of protostars is an important topic in astrochemistry. Since the pioneering work by Cazaux et al. (2003) and Sakai et al. (2008), systematic chemical studies of solar-type protostars (see Ceccarelli et al. 2007; Caselli & Ceccarelli 2012 for a review; also Lefloch et al. 2018) have identified two classes of objects. The first class corresponds to the so-called "hot corinos", that is, sources which display a rich content in complex organic molecules (COMs) in the central inner regions of the protostellar envelope (see Ceccarelli et al. 2007 for a review; also Taquet et al. 2015). Only a few hot corinos have been identified so far either with single dish or interferometric observations: IRAS16293-2422 (Cazaux et al. 2003; Bottinelli et al. 2004b; Jørgensen et al. 2011, 2016), IRAS2, IRAS4B (Bottinelli et al. 2007), IRAS4A (Bottinelli et al. 2004a; Taquet et al. 2015), HH212 (Codella et al. 2016), L483 (Oya et al. 2017), B335 (Imai et al. 2016), SVS13A (Bianchi et al. 2017), Serpens SMM1, and SMM4 (Öberg et al. 2011). We note that very few sources were investigated in a systematic manner meaning that the COM budget in hot corino sources is very inhomogeneous, making a general picture difficult to come by. Hot corinos share some similarities with the hot cores observed around high-mass stars but they are not scaled-down versions of these.

Bottinelli et al. (2007) showed that the abundances of O-bearing species scaled to methanol are higher than those measured in hot cores by one to two orders of magnitude or more. The second chemical class of protostars corresponds to the so-called Warm Carbon Chain Chemistry (WCCC) sources, which have a rich content in C-chains but are poor in COMs. A recent survey of a sample of 36 Class 0/I protostars of the Perseus molecular cloud complex by Higuchi et al. (2018) shows that the majority of the sources observed have intermediate characters between these two distinct chemistry types.

In comparison, very little is known on intermediate-mass (IM) protostars. The first systematic study was carried out by Crimier et al. (2010) and Alonso-Albi et al. (2010), who both investigated the physical and chemical properties of a sample of five Class 0 IM protostars (CB3-mm, Cep E-mm, IC1396 N BIMA 2, NGC 7129 FIRS 2, and Serpens FIRS 1). Crimier et al. (2010) derived the dust and gas temperature and density profiles of the protostellar envelopes from modelling their spectral energy distribution (SED) with the one-dimensional (1D) radiative transfer code DUSTY. Comparing the physical parameters of the envelopes (density profile, size, mass) with those of the envelopes of low- and high-mass protostars led them to conclude that the transition between the three groups appears smooth, and that the formation processes and triggers do not substantially differ. Alonso-Albi et al. (2010) studied the CO depletion and the N_2H^+ deuteration in the same source sample (and additionally towards L1641 S3 MMS1 and OMC2-FIR4). They found hints of CO underabundance by a factor of two with respect to the canonical value in the inner protostellar regions; they pointed out that high-angular-resolution observations are needed to conclude on the origin of such a deficit, and the possible role of outflows and the UV radiation from the star. The chemical properties of the source sample (molecular species and abundances) remain to be fully characterised. A few individual sources have been studied in detail (Fuente et al. 2007; Neri et al. 2007; Hogerheijde et al. 1999; Schreyer et al. 2002). In particular, Fuente et al. (2005) reported the presence of a hot core in NGC 7129 FIRS 2.

Intermediate-mass Class 0 protostellar clusters are important too as they also provide the transition between the low-density groups of TTauri stars and the high-density clusters around massive stars. OMC2-FIR4 is one of the (if not the) best-studied prototypes of this class. OMC-2 FIR4 is itself a young proto-cluster that harbours several embedded low- and intermediate-mass protostars (Shimajiri et al. 2008; López-Sepulcre et al. 2013). Analysis of the CH_3OH emission lines observed with *Herschel* Space Observatory (Pilbratt et al. 2010) in the framework of the CHESS Large Program (Ceccarelli et al. 2010) led Kama et al. (2010) to suggest the presence of a hot core with kinetic temperatures above 100 K and around 400 au in size towards OMC-2FIR4. This is supported by the similarity of the molecular line spectrum of OMC-2 FIR4 and the hot corino source NGC 1333-IRAS4A, as observed with ASAI[1] (Lefloch et al. 2018). Observations with the Northern Extended Millimeter Array (NOEMA) at 5″ resolution by López-Sepulcre et al. (2013) revealed a relatively complex structure with the presence of several components each of one or several solar masses, with chemical differentiation and an ionized HII region just next to the OMC-2 dust envelope. The chemical properties of IM protostars therefore remain to be characterized. The chemical diversity and its similarities and differences with low- and high-mass sources remain to be established.

As part of an observational effort to address these questions, we have conducted a detailed molecular line survey of the isolated IM Class 0 protostar Cep E-mm (IRAS23011+6126) with the IRAM 30 m telescope, complemented with observations with the IRAM interferometer NOEMA. Cep E-mm is located in the Cepheus E molecular cloud at a nearby distance of $d = 730$ pc (Sargent 1977). Its luminosity is $\sim 100\,L_\odot$ and its envelope mass is $35\,M_\odot$ (Lefloch et al. 1996; Crimier et al. 2010). Since its early discovery by Wouterloot & Walmsley (1986) and Palla et al. (1993), subsequent studies have confirmed the source to be an isolated intermediate-mass protostar in the Class 0 stage (Lefloch et al. 1996; Moro-Martín et al. 2001). The source drives a very luminous molecular outflow and jet (Lefloch et al. 2011, 2015), terminated by the bright Herbig-Haro object HH377 (Ayala et al. 2000).

The article is organised as follows. In Sect. 2, we present the observations carried out with the IRAM 30 m telescope and the NOEMA interferometer. In Sect. 3, we present the results on the source multiplicity obtained from the thermal dust emission, as mapped with NOEMA, and the status of the dust components. In Sect. 4, we present the results of a systematic search for COMs, chemically related species with the IRAM instruments, which shows the presence of a hot corino associated with one of the dust components. In Sect. 5, we discuss the physical structure of Cep E-mm and the evidence for chemical differentiation in the core, and we compare our results with those obtained towards a few typical objects, from low- to high-mass. Our conclusions are summarised in Sect. 6.

2. Observations

2.1. Single-dish survey

Observations on Cep E-mm were obtained with the IRAM 30 m telescope near Pico Veleta (Spain) on coordinates $\alpha(2000) = 23^h03^m12^s.8$, $\delta(2000) = 61°42'26''$. Unbiased spectral coverage was carried out at 3 mm (80–116 GHz), 2 mm (129–173 GHz), 1.3 mm (200–300 GHz) and 0.9 mm (330–350 GHz) in Winter 2010 & 2015 and in Summer 2016 using the Eight MIxer Receiver (EMIR). The Fourier Transform Spectrometer (FTS) units were connected to the receivers on the 3 and 2 mm bands, providing a resolution of 195 kHz ($\Delta V \sim 0.6$ and 0.4 km s^{-1} respectively). The Wideband Line Multiple Autocorrelator (WILMA) was connected to the higher-frequency bands, providing a resolution of 2 MHz ($\Delta V \sim 2.5$ and 1.8 km s^{-1} for the 1.3 and 0.9 mm bands respectively). The observations were performed in wobbler switching mode with a throw of 180″(90″ for the 2 mm) in order to ensure a flat baseline. The telescope beam size ranges from 34″ at 72 GHz to 7″ at 350 GHz. Calibration uncertainties in the 3, 2, 1.3 and 0.9 mm bands are typically 10, 15, 20 and 30%, respectively. The data were reduced using the GILDAS-CLASS software[2]. Intensities are expressed in units of antenna temperature corrected for the atmospheric absorption T_A^*. The rms noise per velocity interval of 1 km s^{-1} expressed in units of T_A^* lies in the range 2–5 mK in the 3 mm band, 3–7 mK in the 2 mm and 1.3 mm band, and 15–20 mK in the 0.9 mm band. The spectral bands and observations properties are summarised in Table 1.

[1] http://www.oan.es/asai/

[2] http://www.iram.fr/IRAMFR/GILDAS/

Table 1. IRAM 30 m observational parameters.

Band	Range (GHz)	Backend	Spectral resolution (MHz)	$F_{\rm eff}$	$B_{\rm eff}$	$HPBW$ ($''$)	rms (mK, $T_{\rm A}^*$)
3 mm	72–116	FTS	0.195	0.95	0.81–0.78	34.2–21.2	2–5
2 mm	126–173	FTS	0.195	0.94–0.93	0.72–0.64	19.5–14.2	3–7
1.3 mm	200–310	WILMA	2	0.91–0.82	0.59–0.37	12.3–7.9	3–7
0.9 mm	328–350	WILMA	2	0.82	0.32	7.7–7.0	15–20

Table 2. NOEMA interferometric observations properties.

Band	Range (GHz)	Backend	Spectral resolution (MHz)	Config.	Synthesized beam ($''\times''$)	PA (°)	rms (mJy beam^{-1})
3 mm	85.9–89.6	WideX	2	BC	2.38 × 2.13	60	1–3
	86.0–86.2	Narrow	0.625	BC	2.46 × 2.20	52	3
	86.7–86.9	Narrow	0.625	BC	2.46 × 2.19	48	3
	88.5–88.7	Narrow	0.625	BC	2.39 × 2.07	–133	3
	89.1–89.3	Narrow	0.625	BC	2.36 × 2.06	49	3
1.3 mm	216.8–220.4	WideX	2	CD	1.46 × 1.39	72	3–5
	217.3–217.6	Narrow	0.625	CD	1.42 × 1.41	40	10
	218.7–218.9	Narrow	0.625	CD	1.46 × 1.37	–90	8

2.2. Interferometric observations

The Cep E protostellar region was observed during Winter 2014–2015 with the IRAM NOEMA interferometer at 3 mm and 1.3 mm. At 3 mm, the spectral band 85.9–89.7 GHz covering the SiO J = 2−1 line was observed in B and C configurations on 3 and 12 December 2014 and 6–7 March 2015, in a single field centred at the nominal position of the protostar $\alpha(2000) = 23^{\rm h}03^{\rm m}12\overset{\rm s}{.}8$, $\delta(2000) = 61°42'26''$. At 1.3 mm, the spectral band 216.8–219.95 GHz covering the SiO J = 5−4 line was observed in C and D configurations on 9 December 2014, 7 December 2015, and 13 and 24 April 2015. The 1.3 mm band was observed over a mosaic of five fields centred at offset positions (−9″, −20.8″), (−4.5″, −10.4″), (0″, 0″), (+4.5″, +10.4″) and (+4.5″, +20.8″) with respect to the protostar, in order to map the emission of the protostar and the high-velocity outflow.

The Wideband Express (WideX) backend was connected to the receivers providing a resolution of 2 MHz ($\Delta V \sim 2.7$ km s^{-1} at 1.3 mm). Narrow spectral bands with lines of interest were observed in parallel with a resolution of 256 kHz. Observations properties are summarised on Table 2 for both the Wide Correlator (Widex) and the Narrow correlator backends. The antenna baselines sampled in our observations range from 19 to 176 m at 1.3 mm (from 21 to 443 m at 3 mm), allowing us to recover emission on scales from 14.7 to 1.5″ at the 1.3 mm (from 34 to 1.6″ at 3 mm). At 1.3 mm, for both C and D tracks, phase was stable (rms ≤ 45°) and the precipitable water vapor (pwv) was 1–3 mm with system temperatures ∼100−200, leading to less than 2% flagging in the dataset. At 3 mm, phase rms was ≤50° pwv was 1–10 mm, and system temperatures were ∼60−200 K, leading to less than 1% flagging in the dataset.

Calibration and data analysis were carried out following standard procedures using the GILDAS software[3]. The continuum emission at 1.3 mm and 3 mm was obtained by selecting spectral windows free of molecular line emission. Continuum-free molecular maps were subsequently produced by subtraction of the continuum contribution.

[3] http://www.iram.fr/IRAMFR/GILDAS/

Using a natural weighting, the size of the synthesised beams at 1.3 and 3 mm are 1.46″ × 1.39″ (PA = 72°) and 3.55″ × 2.65″ (PA = 60°), respectively. The uncertainty on the absolute flux calibration is ≤20% and ≤10% at 1.3 and 3 mm respectively; and the typical rms noise per spectral resolution channel is 3–5 mJy beam^{-1} and from 1–3 mJy beam^{-1}.

3. Dust continuum emission

3.1. Source multiplicity

Map of the 1.3 mm continuum emission is displayed in the top panel of Fig. 1. It shows a core of dimensions 1.56″ × 1.08″ (1141×788 au; beam deconvolved), with a PA of 45°. The peak of the flux distribution (99.4 mJy/1.4″-beam) is located at the nominal position of Cep E-mm, and drives the well-known, bright, high-velocity CO outflow (Lefloch et al. 2015). Integrating over the region defined by the 3σ contour level (3.5 mJy/1.4″-beam), the total flux of the condensation is then $S_{1.3\,\rm mm} = 233$ mJy.

The location of the peak flux is shifted with respect to the center of the continuum core, suggesting the presence of a secondary, fainter source located at about 1.7″ southwest of the peak flux. In what follows, we will refer to the first (bright) and secondary (faint) components as Cep E-A and Cep E-B, respectively (Fig. 1).

We determined the position, size and intensity of the two continuum sources from a fit to the visibility table, assuming two 1D Gaussian distributions. We note that the uncertainties correspond to the statistical errors derived from the minimisation procedure. We find that the bright source Cep E-A has a diameter of 1.20″ ± 0.01″ (875 au) (beam-deconvolved) and a peak flux of 97.1 mJy/1.4-beam and a total flux of 168.8 ± 0.7 mJy. The fainter source Cep E-B is located at the offset position (−0.85″, −1.52″), at 1250 au from the Cep E-A. It has a size of 0.92″ ± 0.02″ (670 au). We estimate a peak flux of 26.2 mJy/1.4-beam and a total flux 40.3 ± 0.6 mJy.

In order to elucidate the nature of both condensations, we searched for evidence of outflowing gas motions associated with Cep E-A and Cep E-B using emission maps of the SiO J = 2−1

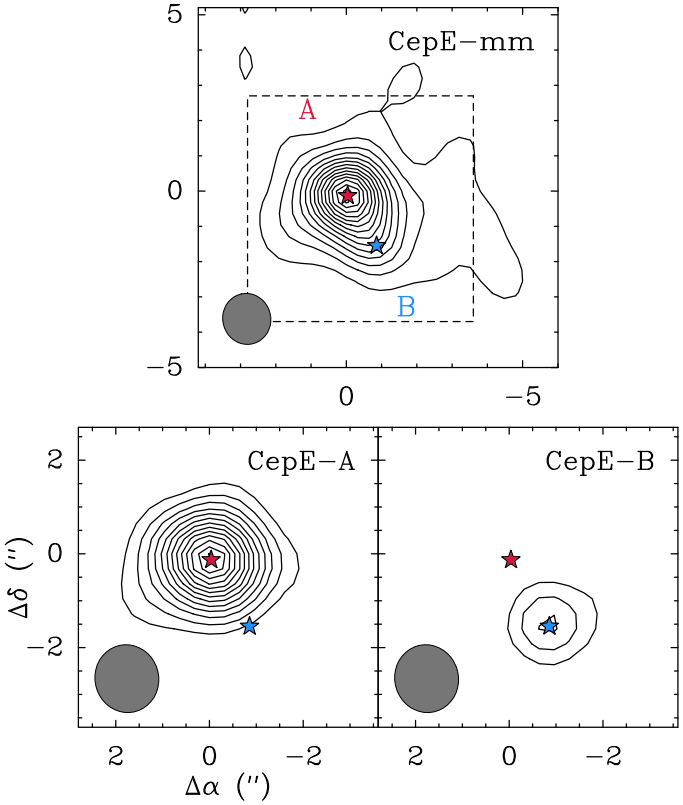

Fig. 1. *Top*: Cep E-mm 1.3 mm continuum map. Base contour and contour spacing are 3.6 (3σ) and 7.2 mJy beam^{-1} (6σ). The peak intensity is 99.2 mJy/1.42″-beam. The blue and red stars mark the position of Cep E-A and B components, respectively. *Bottom*: continuum emission of components A (*left*) and B (*right*) deduced from a two-component fit to the visibilities (see text). Base contour and contour spacing are 10.8 (9σ) and 7.2 mJy beam^{-1} (6σ). Peak intensities are 97.1 and 26.2 mJy/1.42″-beam, respectively.

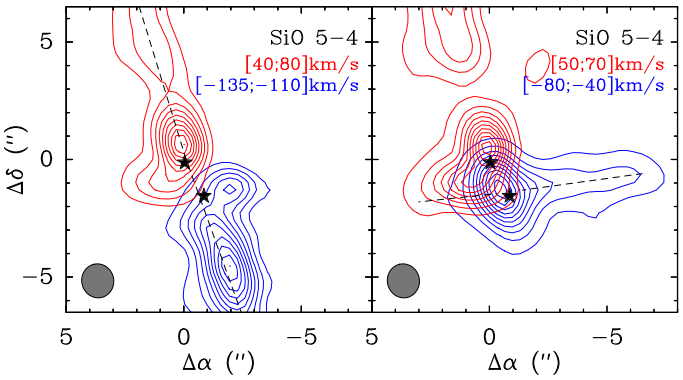

Fig. 2. SiO $J = 5{-}4$ jet emission. The stars points towards the fitted position of both Cep E-A and B cores. *Left*: the blue and red contours represent the integrated line emission between −135 and −110 km s^{-1} and between +40 and +80 km s^{-1}, respectively. Base contour and contour spacing of both jet emission are 10% of their maximum intensity. *Right*: the blue and red contours represent the integrated line emission between −80 and −40 km s^{-1} and between +50 and +70 km s^{-1}, respectively. Base contour and contour spacing of both jet emissions are 5% and 10% of their maximum intensity, respectively.

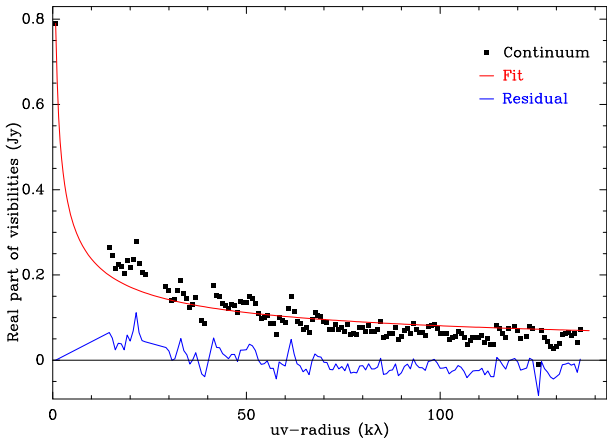

Fig. 3. Continuum (real part of the visibilities, black squares) and corresponding best-fit power-law model (red line) averaged over baseline bins of 1 m, as a function of baseline length. Residuals are shown as a blue line. The zero-spacing 790 mJy flux density is extrapolated from single-dish observations at 1.3 mm by Lefloch et al. (1996).

and 5–4 transitions present in the observed NOEMA bands, a good tracer of young protostellar outflows (Lefloch et al. 1998).

The left hand panel in Fig. 2 shows the SiO $J = 5{-}4$ emission between −135 and −110 km s^{-1} (blue) and +40 and +80 km s^{-1} (red); SiO traces the previously known, high-velocity jet oriented in the southwest-northeast direction (Lefloch et al. 1996, 2011, 2015). Both lobes slightly overlap at the location of Cep E-A, confirming the association with this protostar.

The right hand panel of Fig. 2 displays the SiO $J = 5{-}4$ emission integrated between −80 and −40 km s^{-1} (blue) and +50 and +70 km s^{-1} (red). We note that the redshifted emission is slightly contaminated by the emission from the high-velocity jet from Cep E-A. Overall, the red- and blueshifted emissions draw a collimated, jet-like structure oriented in the eastern-western direction with a PA of −8°. This jet emission is asymmetric, as it appears to be more extended along the blueshifted lobe. Both lobes overlap at about 1.5″ south of Cep E-A. This definitely excludes a possible association with Cep E-A. Instead, the lobes appear to overlap at the position of Cep E-B, supporting a physical association with the secondary dust core.

3.2. Physical properties

The large-scale physical structure of Cep E-mm dust envelope was studied by Crimier et al. (2010). The authors derived the dust density and temperature profiles from a 1D modelling of the dust continuum emission at 24, 70, 450, 850 and 1300 μm by SCUBA and *Spitzer*. Fluxes were measured with an angular resolution in the range 7.5−14.8″, thereby probing mainly the outer regions (>8″) of the envelope. They constrained a power-law index on the density profile $n \propto r^{-p}$ with $p = 1.88$, and obtained self-consistently the temperature profile $T \propto r^{-q}$ with $q = 1.10$ in the inner region ($r < 500$ au). In the Rayleigh-Jeans approximation and for optically thin dust emission, the emergent dust continuum emission also has a simple power-law form $I(r) \propto r^{-(p+q-1)}$. For interferometric observations, the visibility distribution is then $V(b) \propto b^{(p+q-3)}$, and depends only on the density and temperature power-law index.

As can be seen in Fig. 3, a simple fit of the form $V(b) \propto b^{(-0.47\pm0.01)}$ reproduces well our interferometric continuum observations and the single-dish flux of Lefloch et al. (1996). We obtain a $(p + q)$ value of 2.53 ± 0.01 lower than that of Crimier et al. (≃2.98). Such a lower value is consistent with a steeper density profile in the inner regions probed by the interferometer, and could indicate collapse of the inner layers.

Table 3. Physical properties of the Cep E-mm condensation and the components A and B.

Continuum component	Size[a] (″)	Size[a] (au)	Peak Coord. (″)	$S^{\rm beam}_{1.3\,\rm mm}$ (mJy beam^{-1})	$S_{1.3\,\rm mm}$[b] (mJy)	$T_{\rm dust}$[c] (K)	$N(H_2)$ (10^{23} cm^{-2})	$n(H_2)$ (10^7 cm^{-3})	M ($M_\odot$)
Whole core	1.56 × 1.08	1141 × 788	(+0, +0)	99.4	233	55	5.7	4.0	0.83
Cep E-A	1.2	875	(+0, +0)	97.1	168.8	60	5.2	4.0	0.56
Cep E-B	0.9	670	(−0.8, −1.5)	26.2	40.3	25	4.0	4.0	0.38
						60	1.3	1.3	0.13

Notes. [(a)] FWHM, beam-deconvolved. [(b)] Best fit results. [(c)] Based on Crimier et al. (2010). For Cep E-B two $T_{\rm dust}$ are assumed (see text).

In order to estimate the physical parameters of the dust condensation and the protostellar cores Cep E-A and B, we have adopted as dust temperature $T_{\rm dust}$ the value estimated by Crimier et al. (2010) at the core radius (55 K at r = 480 au), and we have adopted a dust mass opacity $\kappa_{1.3\,\rm mm}$ = 0.0089 cm^2 g^{-1} calculated by Ossenkopf & Henning (1994), specifically their OH5 dust model which refers to grains coated by ice. Under these assumptions, we obtain a beam-averaged gas column density N(H_2)= (5.7 ± 1.0) × 10^{23} cm^{-2} in a beam of 1.4″. From this gas column density estimate and the size of the condensation, we obtain the average gas density (nH$_2$) = (4.0 ± 0.8) × 10^7 cm^{-3} for the condensation. This value is in agreement with the gas density derived by Crimier model 4.3 × 10^7 cm^{-3} at the same radius of 480 au. From the integrated flux (233 mJy), we derive the mass of the condensation M = 0.83 ± 0.17 $M_\odot$.

Our NOEMA maps show that the millimeter flux is dominated by Cep E-A. Under the assumption that this source dominates the SED, we can use the Crimier model to estimate the physical parameters of Cep E-A. Proceeding in the same way as above gives $T_{\rm dust}$ ≃ 60 K at the fitted core radius r = 440 au. We obtain N(H_2) = (5.2 ± 1.0) × 10^{23} cm^{-2} and n(H_2) = (4.0 ± 0.8) × 10^7 cm^{-3} and a total dust mass M = 0.5 ± 0.1 $M_\odot$.

For Cep E-B, we constrain an upper temperature limit $T_{\rm dust,max}$ = 60 K similar to that of Cep E-A. A lower limit to $T_{\rm dust}$ is provided adopting the temperature derived in the Crimier model at the radial distance between components A and B (1.7″): $T_{\rm dust}$ = 25 K; hence, we estimate the gas column density N(H_2) = (1.3–4.0) × 10^{23} cm^{-2} the gas density n(H_2) = (1.3–4.0) × 10^7 cm^{-3} and the mass M = (0.13–0.38) $M_\odot$.

The physical properties of both protostars are summarised in Table 3.

4. Complex organic molecules

The first hint on the presence of COMs in Cep E-mm was provided by López-Sepulcre et al. (2015) who reported the presence of formamide (NH_2CHO). Following this study, we have carried out a systematic search for COM emission in the IRAM 30 m survey and the NOEMA observations. We searched for emission lines from the species identified in the solar-type protostar IRAS16293-2422 (Cazaux et al. 2003; Jaber et al. 2014) and the protostellar shock L1157-B1 (Lefloch et al. 2017). Line identification was carried out using the WEEDS package in GILDAS (Maret et al. 2011) and the public databases CDMS (Müller et al. 2005) and JPL (Pickett et al. 1998).

4.1. Content

The following complex O-bearing and N-bearing organic species are detected towards the Cep E-mm protostellar envelope: methanol (CH_3OH) and its rare isotopologues $^{13}CH_3OH$ and CH_2DOH, acetaldehyde (CH_3CHO), dimethyl ether (CH_3OCH_3), methyl formate ($HCOOCH_3$), Acetone (CH_3COCH_3), formamide (NH_2CHO), methyl cyanide (CH_3CN) and ethyl cyanide (C_2H_5CN). The number of lines detected with both instruments and the range of upper-level energies $E_{\rm up}$ (K) are given in Table 4. A montage of illustrative transitions from each species observed with the IRAM 30 m telescope is displayed in Fig. 4. In this work, we also report the detection of the following species, chemically related to COMs: formaldehyde (H_2CO), ketene (H_2CCO), formic acid (HCOOH), isocyanic acid (HNCO).

Because of the limited spectral coverage of NOEMA observations and the lower sensitivity of the IRAM 30 m survey, there is only a partial match between the sets of detected lines detected with both instruments. We note that, apart from CH_3CN (not observed with NOEMA), Propanone (CH_3COCH_3) and Ethyl Cyanide (C_2H_5CN) were not detected by the IRAM 30 m telescope; and Vinyl cyanide (C_2H_3CN) was not detected by NOEMA. Our NOEMA observations show bright emission from highly excited molecular transitions, like $HCOOCH_3$ $20_{0,20}$–$19_{0,17}$ ($E_{\rm up}$ = 111.5 K) or CH_3OH-A $6_{1,-1}$–$7_{2,-1}$ ($E_{\rm up}$ = 373.9 K) which are not detected with the IRAM 30 m. This effect results from the dilution of the emission in the telescope main beam.

In order to estimate the amount of flux filtered out by NOEMA, we compared the fluxes of molecular transitions detected at ⩾5σ. The results obtained are summarised in Table 5. We found that all the flux is recovered for lines from high $E_{\rm up}$, like CH_3OH $8_{0,0}$–$7_{1,0}$ ($E_{\rm up}$ = 88.7 K). For the other transitions of lower excitation, the interferometer recovered from 20 to 60% of the flux collected with the IRAM 30 m. This is illustrated in the case of H_2CO J = $3_{0,3}$–$2_{0,2}$ ($E_{\rm up}$ = 21 K), CH_3OH J = $4_{2,0}$–$3_{1,0}$ ($E_{\rm up}$ = 45.5 K) and HNCO $10_{0,10}$–$9_{0,9}$ ($E_{\rm up}$ = 58.0 K) in Fig. 5.

4.2. Spectral signatures

Figure 4 shows that a large variety of profiles is observed, depending on the molecular species and the line excitation conditions. For instance, narrow line components (≃1–3 km s^{-1}) peaking at the cloud systemic velocity ($v_{\rm lsr}$ = −10.9 km s^{-1}) are detected in HCOOH and CH_3CHO. Broad velocity components extending over 20 km s^{-1} are also detected in the profiles of H_2CCO or CH_3CHO. We have identified three types of spectral line features, depending on the line width, the velocity range, and the emission peak velocity: a narrow line component (NL), a broad line component (BL), and the extremely broad line component (eBL).

The three components are detected in the low-excitation transitions of methanol, with $E_{\rm up}$ < 50 K. The eBL and BL components are both found in transitions up to $E_{\rm up}$ < 100 K, whereas only the BL component is detected in higher excitation transitions with $E_{\rm up}$ > 100 K. This is shown in Fig. 6 in which we report the line width of each component as a function of the upper energy level $E_{\rm up}$ for all methanol transitions, as

Table 4. Molecular species (COMs and chemically related species) detected with the IRAM 30 m telescope and the NOEMA interferometer.

Species	30 m					NOEMA			
	n	E_{up} (K)	Components			n	E_{up} (K)	Components	
			eBL	BL	NL			eBL	BL
E-CH_3OH	72	4.6–500.5	×	×	×	4	37.6–500.5	×	×
A-CH_3OH	64	7.0–446.5	×	×	×	2	373.9–745.6		×
$^{13}CH_3OH$	21	6.8–113.5		×		1	162.4		×
CH_2DOH	36	6.2–123.7		×	×	4	10.6–58.7	×	×
H_2CO	15	3.5–125.8	×	×	×	3	21.0–68.1	×	×
$H_2^{13}CO$	9	10.2–61.3	×	×	×	1	32.9	×	×
H_2CCO	18	9.7–102.1		×	×	1	76.5	×	×
HCOOH	6	10.8–23.5			×	1	58.6		×
$HCOOCH_3$	24	20.1–111.5		×		16	20.1–111.5		×
CH_3CHO	63	7.6–89.8	×		×	1	18.3		×
CH_3OCH_3	30	11.1–106.3		×		1	253.4		×
CH_3COCH_3	0					1	119.1		×
HNCO	18	10.5–82.3	×		×	3	58.0–231.1	×	×
NH_2CHO^a	6	10.2–22.1			×	1	60.8		×
CH_3CN	38	8.8–148.6		×	×	*			
C_2H_5CN	0					2	135.6–139.9		×

Notes. For each species, we indicate the number n of detected transitions, the corresponding range of E_{up} and the detected spectral component with the 30 m: extremely broad line (eBL) component, the broad line (BL) component, and the narrow line (NL) component. [(a)] 30 m lines from López-Sepulcre et al. (2015). [(*)] No transition present in the band.

derived from a Gauss fitting to the line profiles. Figure 7 shows three methanol transitions with E_{up} = 28 K, 70 K, and 110 K, respectively, observed in the 2 mm band at approximately the same angular resolution (15.8″). It turns out that the low- and mid-excitation line methanol emission (E_{up} = 28 K and 70 K) is dominated by the contribution of the extremely broad line component, whereas the high-excitation line emission is dominated by the BL component.

We have applied the same decomposition to the line profiles of the other detected molecular species that are listed in Table 4. We describe their properties in more detail hereafter.

4.2.1. The extremely broad line (eBL) component

Methanol spectra show an eBL with a line width (FWHM) $\Delta v \geqslant 7\,\mathrm{km\,s^{-1}}$ (Fig. 6) and peaking at velocities up to $\pm 10\,\mathrm{km\,s^{-1}}$ with respect to the source ($v_{lsr} = -10.9\,\mathrm{km\,s^{-1}}$). The line emission can be reasonably well fitted by a Gaussian centred at a velocity shifted by 1–3 $\mathrm{km\,s^{-1}}$ from the source (Fig. 7, top and middle panel; also Fig. 4). It is detected in the transitions with $E_{up} \leq 100$ K, only. This component is detected with NOEMA and traces the cavity walls of the high-velocity outflow driven by Cep E-A. We estimate a typical size of 20″ (see Lefloch et al. 1996, 2015). This component is also detected in the lines of formaldehyde, methyl cyanide, and acetaldehyde (see Table 4).

4.2.2. The narrow line (NL) component

An NL $\Delta v \leqslant 3\,\mathrm{km\,s^{-1}}$ peaking at the systemic velocity of the cloud, is detected only in the profiles of the low-excitation CH_3OH lines ($E_{up} \leq 50$ K). This component is present in the line spectra of many COMs (CH_3CHO, HCOOH, CH_3CN, and H_2CCO) with $E_{up} \leq 60$ K, when observed with the IRAM 30 m. The flux filtered by the interferometer is about 60–80% for these transitions (see Table 5). We note that the low velocity dispersion and the low excitation conditions of this gas component are consistent with an origin in the cold and quiescent outer envelope.

4.2.3. The broad line (BL) component

The BL is seen in all the methanol transitions detected with IRAM 30 m. This component differs from the bipolar outflow as (a) its emission peaks at the source systemic velocity, (b) its linewidth varies little with E_{up}, and (c) it is detected in the high-excitation lines of methanol, with E_{up} in the range 100–500 K (see Tables A.1 and A.2). We find a very good match between the high-excitation line profiles of methanol observed with the NOEMA and those observed with the IRAM 30 m. This confirms that we are actually detecting the same component. Interestingly, the line profiles of COMs, as observed with NOEMA, can be well fitted by a Gaussian with a line width of $\simeq 5\,\mathrm{km\,s^{-1}}$, similar to that of the high-excitation CH_3OH lines.

4.3. Spatial distribution

We have produced emission maps of selected molecular transitions of COMs and chemically related species from the calibrated UV table adopting a natural weight. A montage of such maps is shown in Fig. 8. The emission of the various COMs appears to be compact and centred on the dust emission peak of Cep E-A. Interestingly, there is no molecular emission centered on Cep E-B, the second core component.

We have estimated the size of the COM emission region around Cep E-A for the following bright molecular lines: CH_3OH $5_{1,0}$–$4_{2,0}$ and $6_{1,5}$–$7_{2,6}$, CH_2DOH $5_{1,5}$–$4_{1,4}$ and $HCOOCH_3$ $20_{0,20}$–$19_{0,19}$. We performed 1D Gaussian fits to the visibilities in the UV plane around the Cep E-A. The result of the procedure does not appear to depend significantly on the E_{up} of the transition, which ranges between 36 and 112 K. We obtained a typical size of 0.7″ ± 0.1″(FWHP) for all the transitions, that is, the emission region is marginally resolved.

As can be seen in Fig. 8, the emission of H_2CO $3_{2,2}$–$2_{2,1}$ (E_{up} = 68 K) appears slightly more extended than that of CH_2DOH and other COMs. A fit to the H_2CO $3_{2,2}$–$2_{2,1}$ distribution yields a size of 1.2″. For COMs like CH_3OCH_3,

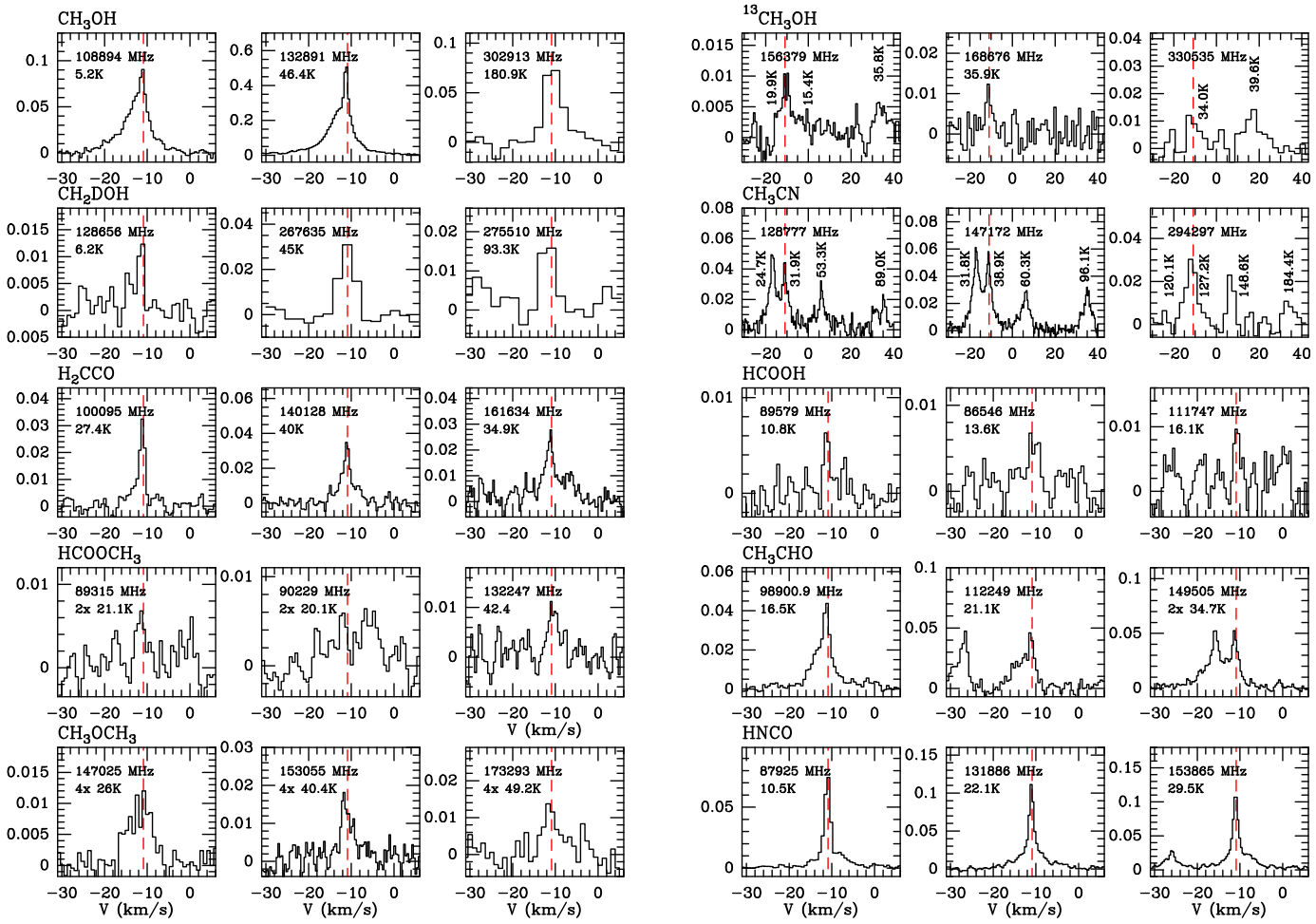

Fig. 4. Montage of detected transitions from COMs and chemically related species towards Cep E-mm with IRAM 30 m. Intensities are expressed in units of $T_{\rm A}^{*}$. The red dashed line marks the ambient cloud velocity $v_{\rm lsr} = -10.9\,{\rm km\,s^{-1}}$.

Table 5. Fluxes of molecular transitions detected at $\geqslant 5\sigma$ recovered by NOEMA and compared to the 30 m telescope.

Species	Frequency (MHz)	Quantum numbers	$E_{\rm up}$ (K)	Recov. (%)
CH_3OH	218 440	$4_{2,0}-3_{1,0}$	37.6	60
	216 946	$5_{1,0}-4_{2,0}$	48.0	50
	220 079	$8_{0,0}-7_{1,0}$	88.7	90
CH_2DOH	86 669	$2_{1,1,0}-2_{0,2,0}$	10.6	20
H_2CO	218 222	$3_{0,3}-2_{0,2}$	21.0	30
	218 760	$3_{2,1}-2_{2,0}$	68.1	60
HNCO	219 798	$10_{0,10}-9_{0,9}$	58.0	50

CH_3COCH_3, and H_2CCO $3_{0,3}$–$2_{0,2}$, the intensity of the detected lines is much lower and the results of a UV visibility fitting procedure are too uncertain. In such cases, we estimated the size of the emitting region directly from a simple Gaussian fit to integrated intensity maps, deconvolved from the synthesized beam (1.4″). The results display relatively little scatter, and we find sizes ranging between 0.6 and 0.8″.

We note that the emission of the low $E_{\rm up}$ transitions of CH_3OH, H_2CO, and HNCO also trace an extended component associated with the cavity walls of the outflow system (Lefloch et al. 2015).

To summarise, our NOEMA observations provide direct evidence for a hot corino region around Cep E-A. Estimates of the emitting regions of various COMs yield a typical size of about 0.7″, with little scatter. This size is close to the half power beam width of the synthetic beam, meaning that the hot corino region is only marginally resolved.

4.4. Molecular abundances in Cep E-A

In this section, we discuss the physical properties (excitation temperature, column densities) of the COMs and the chemically related species detected towards the hot corino of Cep E-A. The hot corino properties were obtained from a population diagram analysis of their spectral line energy distribution (SLED) or under the assumption of local thermodynamical equilibrium (LTE) when only one line was detected, as is the case for CH_3CHO, CH_3COCH_3, HCOOH, NH_2CHO, C_2H_5CN and HNCO. The source size, as determined in Sect. 4.2, was taken into account and the derived column densities are source averaged. In our population diagram analysis, line opacities are taken into account following the approach of Goldsmith & Langer (1999). Under the LTE assumption, in the absence of constraints on the excitation temperature, calculations were done for the following excitation temperatures $T_{\rm ex}$: 30 K and 60 K. The first value is similar to the determinations of $T_{\rm rot}$ of COMs obtained when a population diagram analysis was feasible (see below; also Table 6),

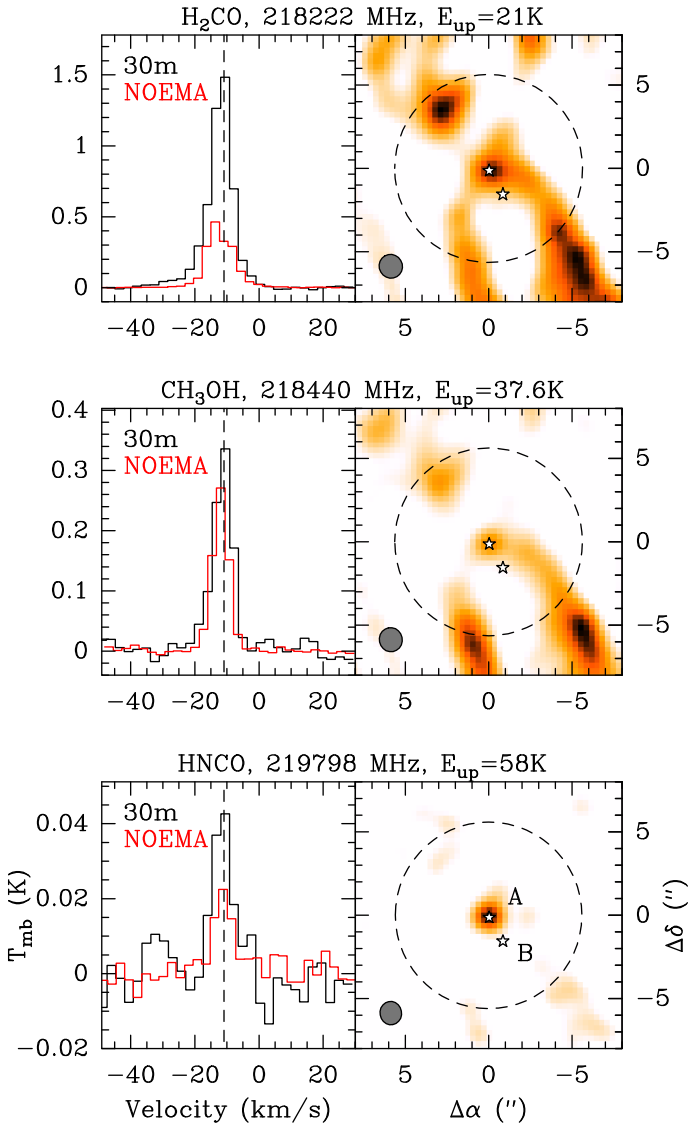

Fig. 5. H_2CO $3_{0,3}$–$2_{0,2}$, CH_3OH $4_{2,0}$–$3_{1,0}$ and HNCO $10_{0,10}$–$9_{0,9}$ transitions detected with both IRAM 30 m and NOEMA towards Cep E-mm. *Left*: 30 m spectra (black) and NOEMA spectra convolved to the single-dish beam (red). Both spectra are displayed with the same spectral resolution. The black dashed line marks the cloud velocity $v_{lsr} = -10.9$ km s^{-1}. *Right*: emission map obtained with NOEMA. The interferometric synthesised beam is represented by the grey disc. White star marks the observing position of the 30 m and the beam width at half-power is drawn by a black dashed circle. The locations of protostars Cep E-A and Cep E-B are marked by stars.

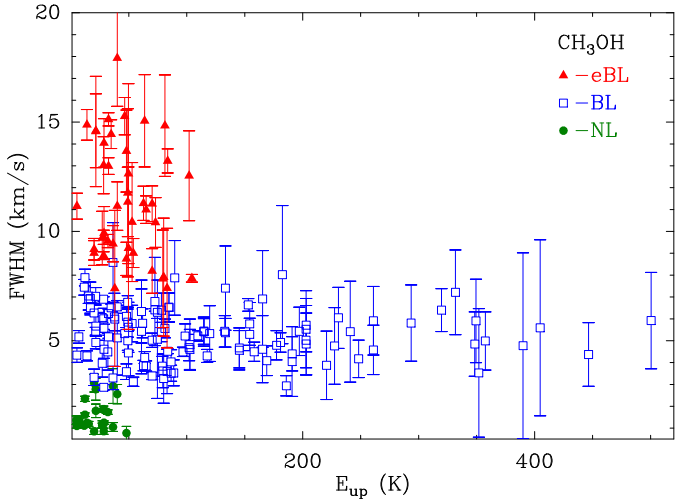

Fig. 6. Linewidth of the three physical components identified in the CH_3OH transitions as a function of the E_{up}.

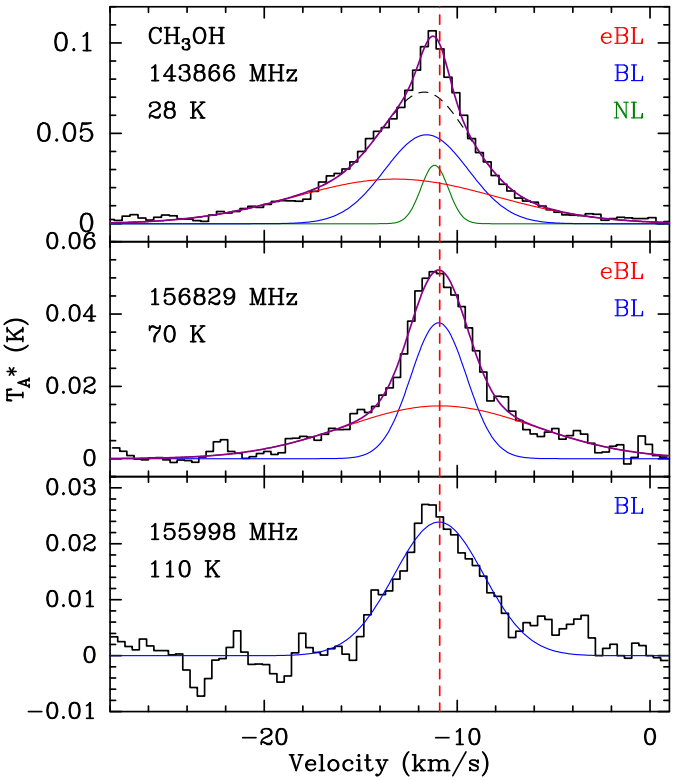

Fig. 7. Methanol line profiles as observed with IRAM 30 m with an angular resolution of 15.8″. The ambient cloud velocity ($v_{lsr} = -10.9$ km s^{-1}) is marked by the dashed red line. *Top*: A-CH_3OH $J = 3_{1,+0}$–$2_{1,+0}$ ($E_{up} = 28.3$ K) transition. Three Gaussian components are fitted to the line profile: the eBL in red, the BL in blue and the NL in green. Dashed black curve shows the sum of eBL and BL components. In purple the overall fit. *Middle*: E-CH_3OH $J = 7_{0,0}$–$7_{-1,0}$ ($E_{up} = 70.2$ K) transition. Only the eBL (red) and BL (blue) components are detected. *Bottom*: E-CH_3OH $J = 9_{0,0}$–$9_{-1,0}$ ($E_{up} = 109.6$ K) transition. Only the BL (blue) component is detected.

while the second value is consistent with the gas kinetic temperature predicted at the hot corino radius by Crimier et al. (2010; see also below Sect. 5.1). In that way, we obtain a plausible range of values for molecular column densities. For the molecular species detected with NOEMA, the SLED was directly measured from the WideX spectra at the location of Cep E-A. For the IRAM 30 m data, we first applied the spectral decomposition discussed in Sect. 4.2 in order to obtain the flux of the three physical components (bipolar outflow, cold envelope, hot corino) and then built the SLED of the hot corino. The list of all the identified transitions, along with their spectroscopic and observational properties are given in Appendix A. We have adopted a hot corino size of 0.7″ for all the COMs and of 1.2″ for $H_2^{13}CO$, in agreement with our NOEMA observations.

The rotational diagrams for E-/A-CH_3OH, $^{13}CH_3OH$, CH_2DOH, $H_2^{13}CO$, CH_3OCH_3, and CH_3CN are presented in Fig. 9. We have superimposed the flux obtained with NOEMA. Molecular abundances were derived adopting a total H_2 column density $N(H_2) = 4.0 \times 10^{23}$ cm^{-2} based on our continuum

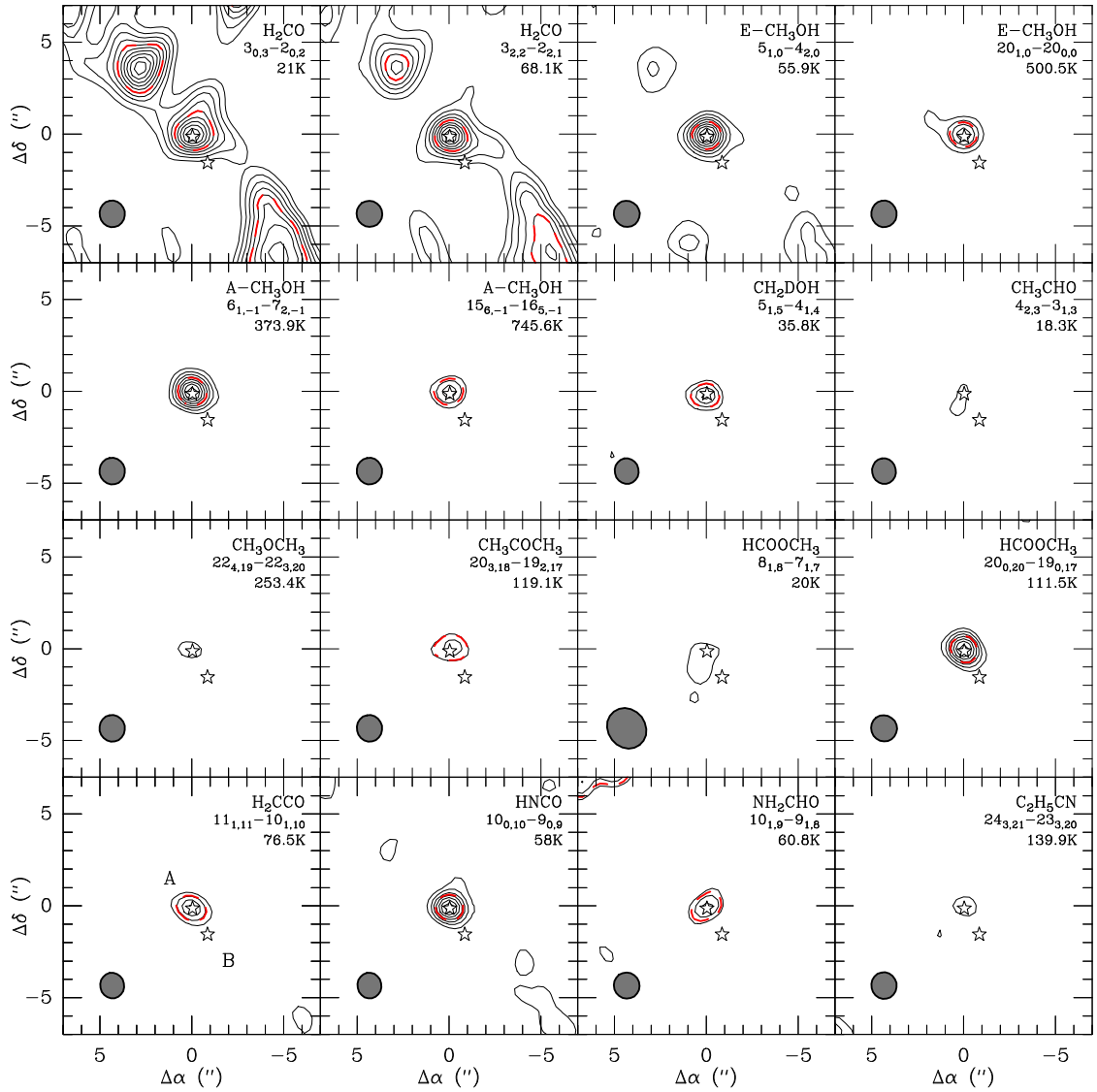

Fig. 8. Integrated emission maps of COMs and chemically related species. For H_2CO, base contour and contour spacing are 10% of the maximum integrated intensity. For the E-CH_3OH map, base contour and contour spacing are 3σ. For the others molecules, base contour and contour spacing are 3 and 2σ of each map. Red-dashed lines corresponds to half maximum intensity if it is greater than 3σ noise. The locations of Cep E-A and Cep E-B are marked by stars.

emission analysis (see Sect. 5.1). The results of our analysis (rotational temperature, source-averaged column density, and molecular abundances relative to H_2) are presented in Table 6.

4.4.1. Methanol

The population diagrams for A-/E-CH_3OH are displayed in Fig. 9; they deviate strongly from linearity meaning that the SLED cannot be fitted by a single rotational temperature. The presence of excitation gradients in the source, line opacity effects, and radiative pumping (see e.g. Leurini et al. 2016) could account for this behaviour. We estimated the opacity of a few CH_3OH transitions detected in the IRAM 30 m survey. We compared the main-beam temperatures of two sets of CH_3OH and $^{13}CH_3OH$ transitions of similar excitation, $3_{0,+}$–$2_{0,+}$ (E_{up} = 14 K) and $5_{2,-}$–$4_{2,-}$ (E_{up} = 73 K) adopting a typical $^{12}C/^{13}C$ abundance ratio of 70 (Langer 1992) and under the standard approximation that both molecules share a similar excitation temperature. We find $\tau^{12} \simeq 3$ (20) for the $3_{0,+}$–$2_{0,+}$ ($5_{2,-}$–$4_{2,-}$) transition. We conclude that the CH_3OH emission is optically thick over a wide range of excitation conditions. Unlike the main isotopologue, the rotational diagrams of CH_2DOH and $^{13}CH_3OH$ are well fitted by a single temperature component.

The population diagram analysis of $^{13}CH_3OH$ yields $N(^{13}CH_3OH) = (7.0 \pm 2.2) \times 10^{15}$ cm^{-2} and $T_{rot} = (27.3 \pm 5.3)$ K. The opacities of the detected $^{13}CH_3OH$ transitions were computed under LTE conditions, and were all found to be $\tau^{13} \leqslant 0.2$, therefore optically thin. As a consequence, we used the optically thin $^{13}CH_3OH$ emission to determine the total methanol column density. Assuming a $^{12}C/^{13}C$ abundance ratio of 70, we obtain the total methanol column density $N(CH_3OH) = (4.9 \pm 1.5) \times 10^{17}$ cm^{-2}.

Six and eight transitions of A- and E-CH_3OH, respectively, with $E_{up} > 200$ K were detected in the IRAM survey. The flux of these transitions cannot be accounted for by the component detected in the $^{13}CH_3OH$ lines, and requires higher excitation conditions. A simple population diagram analysis in the range E_{up} = 150–500 K, yields $T_{rot} = 440 \pm 210$ K, $N = (1.3 \pm 0.4) \times$

Table 6. Physical properties of the molecular emission detected towards Cep E-A.

Species	T_{rot} (K)	N (10^{15} cm^{-2})	X (10^{-9})
$^{13}CH_3OH$	27.3 ± 5.3	7.0 ± 2.2	17.5 ± 5.5
CH_2DOH	20.2 ± 1.2	17.7 ± 2.5	44.3 ± 6.3
$H_2^{13}CO$	14.0 ± 2.4	0.5 ± 0.2	1.3 ± 0.5
H_2CCO	19.6 ± 1.2	3.2 ± 0.5	8.0 ± 1.3
CH_3OCH_3	37.9 ± 1.9	14.4 ± 1.5	36.0 ± 3.8
$HCOOCH_3$	29.8 ± 6.8	10.2 ± 2.5	25.5 ± 6.2
HCOOH	30	0.32 ± 0.12	0.8 ± 0.3
	60	0.34 ± 0.13	0.9 ± 0.3
CH_3CHO	30	4.1 ± 1.0	10.3 ± 2.5
	60	5.0 ± 1.2	12.5 ± 3.0
CH_3COCH_3	30	3.3 ± 0.8	8.3 ± 2.0
	60	1.0 ± 0.2	2.5 ± 0.5
HNCO	30	0.64 ± 0.15	1.6 ± 0.4
	60	0.64 ± 0.15	1.6 ± 0.4
NH_2CHO	30	0.18 ± 0.04	0.5 ± 0.1
	60	0.18 ± 0.04	0.5 ± 0.1
CH_3CN	32.2 ± 4.4	1.4 ± 0.5	3.5 ± 1.2
C_2H_5CN	30	0.42 ± 0.18	1.1 ± 0.5
	60	0.18 ± 0.07	0.5 ± 0.2

Notes. Columns are: rotational temperature, column density, and molecular abundances relative to H_2. An H_2 column density of 4.0×10^{23} cm^{-2} was adopted (see text). A source size of 1.2″ and 0.7″ was assumed for $H_2^{13}CO$ and the other COMs emission, respectively.

10^{16} cm^{-2} and T_{rot} = 460 ± 220 K, $N = (4.2 \pm 1.1) \times 10^{16}$ cm^{-2} for A- and E-species, respectively. One might note a discrepancy between the column densities of E- and A-CH_3OH. However, taking into account the uncertainties on the derived column densities, both estimates are consistent within the 2σ level. The total CH_3OH column density is $N \sim 5 \times 10^{16}$ cm^{-2}, which is one order of magnitude less than the amount of CH_3OH traced by the rare isotopologues. Observations at high angular resolution and better sensitivity would help to clarify the nature of this component.

4.4.2. Other COMs and chemically related species

The population diagrams for the other COMs and some chemically related species ($H_2^{13}CO$, H_2CCO, CH_3OCHO,CH_3OCH_3, CH_3CN and HC_3N) are presented in Fig. 9. As for $^{13}CH_3OH$, the population diagrams are reasonably well fitted by a straight line.

As can be seen in Table 6, all COMs display rather similar rotational temperatures in the range T_{rot} = 20–40 K. No trend is observed as a function of the rotational dipole moment, which is not unusual (see e.g. Lefloch et al. 2017). The H_2CO physical properties were estimated from its ^{13}C isotopologue the same procedure as for CH_3OH. We obtain the total formaldehyde column density $N(H_2CO) = (3.5 \pm 1.4) \times 10^{16}$ cm^{-2}.

Because of the limited spectral coverage of the NOEMA observations, we could only detect one transition from a few COMs (see Table 4). As explained above, the column density and the molecular abundance were estimated for T_{ex} = 30 K and T_{ex} = 60 K. Whereas the first value is similar to the T_{rot} values of COMs obtained from a population diagram analysis (see below; also Table 6), the second value is consistent with the gas kinetic temperature predicted at the hot corino radius by Crimier et al. (2010; see also below Sect. 5.1). This procedure allows us to derive a range of column densities along with their uncertainties. As for HCOOH, CH_3CHO, HCNO, and NH_2CHO, the results do not vary significantly with the adopted value of T_{ex} , and the differences lie within the statistical uncertainties. For these species, in Table 8 we have reported, as abundance, the average results between the 30 and 60 K values. On the contrary, in the cases of CH_3COCH_3 and C_2H_5CN, large differences, up to a factor of three, are found when T_{ex} varies from 30 to 60 K. For these species, we have reported the range of obtained values in Table 8. We have also reported in Table 9 the molecular abundances of COMs relative to that of $HCOOCH_3$, a molecule which is often detected in young stellar objects (see e.g. Lefloch et al. 2018).

The molecular column densities of O-bearing species are found to be relatively similar, of the order of a few times 10^{15} cm^{-2}, except for HCOOH which is less abundant by one order of magnitude. By comparison, N-bearing species (CH_3CN, C_2H_5CN) are less abundant with column densities lower than 10^{15} cm^{-2}. We note that NH_2CHO and HNCO, which both display a peptide bond NH–C=O, harbour abundances similar to N-bearing species.

To summarise, a simple population diagram analysis towards Cep E-A reveals a rich and abundant content in COMs, typical of hot corinos. This is the first detection of a hot corino around an isolated intermediate-mass protostar.

Table 7. Physical properties of the source sample.

Source	d (pc)	L ($L_\odot$)	M ($M_\odot$)	Size (au)
IRAS4A[a]	235	9.1	5.6	48
IRAS16293[b]	120	22	2	120
IRAS2A[a]	235	36	5.1	80
Cep E-A	730	100	35	510
NGC 7129[c]	1250	500	50	760
G29.96[d]	6000	9×10^4	2500	3300
Orion KL[d]	450	10^5	140	560
SgrB2(N)[e]	7900	8.6×10^5	3–10 × 10^4	2×10^4

Notes. Columns are: distance d, bolometric luminosity L, envelope mass M and the hot corino (hot core) region size. [(a)] Taquet et al. (2015), [(b)] Jaber et al. (2014), [(c)] Fuente et al. (2005), [(d)] Beuther et al. (2009), [(e)] Belloche et al. (2013).

5. Discussion

5.1. Physical structure of Cep E-mm

Our observations with NOEMA have shown evidence for a system of two protostars in the dust condensation associated with Cep E-mm. This is consistent with the work by Moro-Martín et al. (2001), who reported hints of multiplicity in Cep E-mm. These authors detected two sources in the dust core observed at 222 GHz, whose coordinates are in good agreement with those of Cep E-A and Cep E-B. They derived the physical parameters of both sources assuming a lower dust temperature (18 K) and dust mass opacity (κ = 0.005 cm^{-2} g^{-1}) than the values adopted here. This results in a higher envelope mass 13.6 $M_\odot$ and higher cores masses of 2.5 and 1.8 $M_\odot$ for Cep E-A and Cep E-B, respectively. Taking into account their hypothesis on T_{dust} and κ, our mass estimates are in good agreement with theirs.

As discussed in Sect. 5.1, we adopted a dust temperature T_{dust} = 55 K and dust mass opacity $\kappa_{1.3\,mm}$ = 0.0089 cm^{-2} g^{-1}

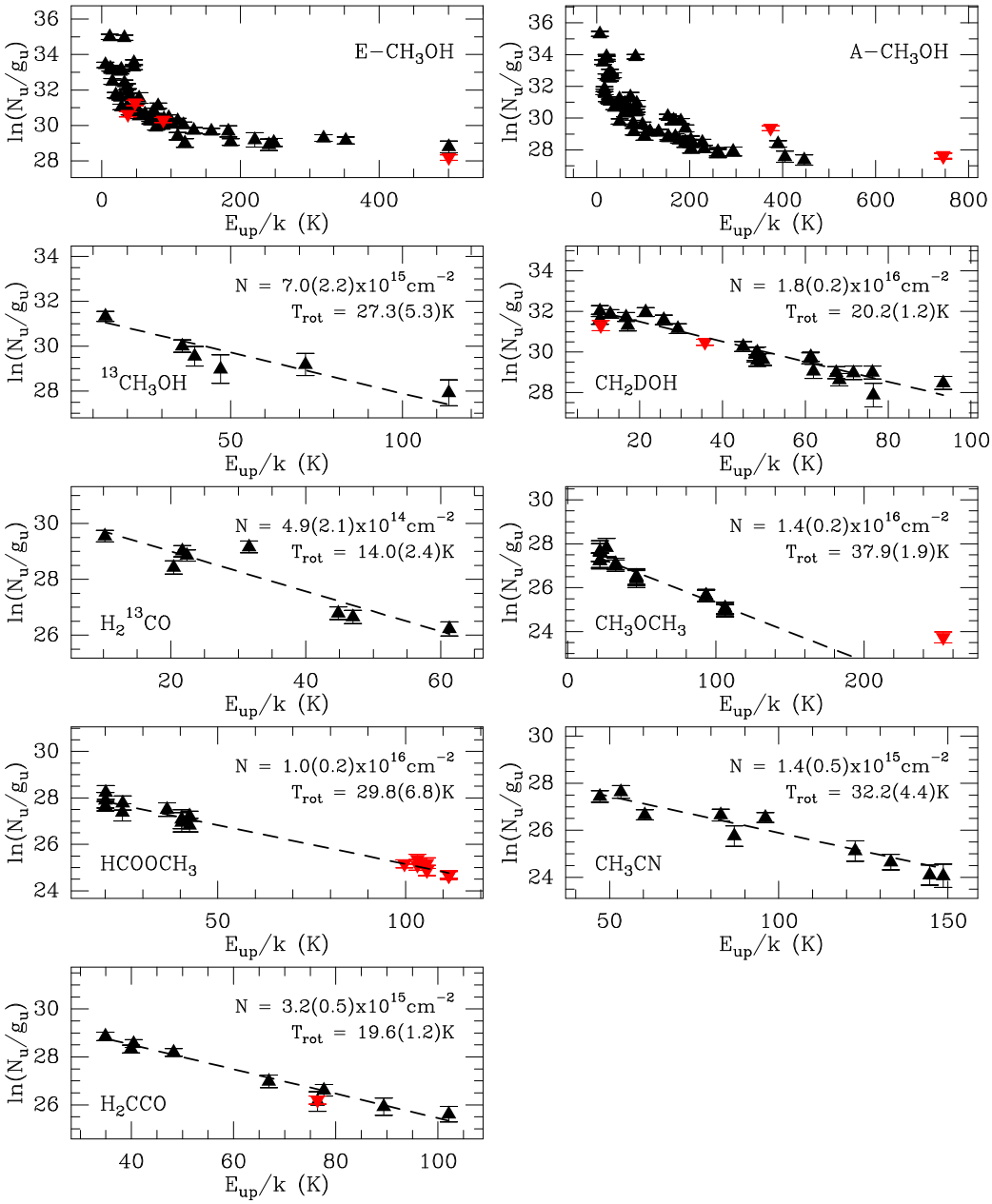

Fig. 9. Population diagram analysis of the COMs detected in the hot corino of Cep E-A. A size of 0.7″ was assumed, except for $H_2^{13}CO$ (1.2″). Black (red) triangles represent the IRAM 30 m (NOEMA) fluxes. The best fitting solution using only the 30 m fluxes is drawn as a black dashed line.

in a region of 950 au (1.3″), corresponding to the mean size of the Cep E-mm condensation. We derived a mean gas density $n(H_2) = (4.0 \pm 0.8) \times 10^7$ cm^{-3} which is in excellent agreement with the value predicted by Crimier et al. (2010). Our continuum observations are therefore consistent with the presence of warm dust and gas at 0.7″ scale around Cep E-A. However, NOEMA reveals CepE-mm to be a binary system and the spherical symmetry hypothesis is no longer valid at 1.7″ scale, the separation between both components (Fig. 1).

5.2. Chemical differentiation

Our COM emission maps show that the flux distributions are strongly peaked towards Cep E-A, while there is barely any molecular emission detected towards Cep E-B (Fig. 8). Many of the COM transitions detected towards Cep E-A are rather weak and are sometimes marginally detected (see Table A.5). Since component B displays a smaller size and a lower gas column density, it is worth investigating whether the apparent chemical differentiation could be biased by the sensitivity of the data. We have applied a simple scaling to the intensities of the COM transitions detected towards Cep E-A, taking into account the difference of the continuum source size and peak flux. This provides a reasonable approximation to the line fluxes towards Cep E-B assuming that the rotational temperature and the physical conditions are the same. We find that five transitions of methanol and two of HNCO should be measured above 5σ noise level but only the brightest methanol transition is detected towards Cep E-B. For all other COMs, the expected intensity then falls under the 3σ detection limit. Only the lack of CH_3OH towards Cep E-B pro-

Table 8. Molecular abundances with respect to H_2 measured towards Cep-E A and a few protostars of low- (LM), intermediate- (IM) and high-mass (HM) reported from the literature.

Molecule	X							
	LM			IM		HM		
	IRAS4A2[a]	IRAS16293B[b]	IRAS2A[a]	Cep E-A	NGC 7129[c]	G29.96[d]	Orion KL[e]	SgrB2(N1)[f]
CH_3OH	4.3 (−7)	1.7(−6)	1.0(−6)	1.2(−6)*	1.0(−6)*	6.7(−8)	9.3(−8)	1.4(−6)
H_2CO	8.2 (−9)	1.6(−7)	8.0(−8)	8.8(−8)*	2.0(−8)*	–	–	3.9(−8)
H_2CCO	9.2 (−10)	–	1.4(−9)	8.0(−9)	–	–	9.3(−12)	4.6(−8)
HCOOH	(0.6–2.9)(−9)	–	–	8.3(−10)	3.0(−8)*	–	1.3(−10)	1.2(−9)
$HCOOCH_3$	1.1(−8)	3.3(−8)	1.6(−8)	2.6(−8)	2.0(−8)	1.3(−8)	4.4(−9)	3.4(−8)
CH_3CHO	(1.1–7.4)(−9)	5.8(−9)	–	1.1(−8)	2.0(−9)	–	1.3(−11)	1.1(−8)
CH_3OCH_3	1.0(−8)	–	1.0(−8)	3.6(−8)	1.0(−8)	3.3(−8)	2.6(−9)	1.5(−7)
CH_3COCH_3	–	1.4(−9)	–	(2.5–8.3)(−9)	5.0(−10)	–	–	1.2(−8)
HNCO	(0.3–1.4)(−9)	2.5(−9)	–	1.6(−9)	8.0(−10)	–	1.9(−9)	1.0(−7)
NH_2CHO	(1.2–6.7)(−10)	8.3(−10)	2.4(−9)	4.5(−10)	–	–	1.9(−10)	1.0(−7)
CH_3CN	(0.3–1.4)(−9)	3.3(−9)	4.0(−9)	3.5(−9)	6.0(−9)*	1.7(−9)	8.5(−10)	1.5(−7)
C_2H_5CN	(1.7–5.6)(−10)	3.0(−10)	3.0(−10)	(0.45–1.1)(−9)	1.4(−9)	1.7(−9)	1.3(−9)	1.4(−7)

Notes. Sources are ordered from left to right by increasing luminosity. [(*)] Obtained from the ^{13}C isotopologue. [(a)] López-Sepulcre et al. (2017), Taquet et al. (2015), [(b)] Jørgensen et al. (2016), Coutens et al. (2016), Lykke et al. (2017), Calcutt et al. (2018), [(c)] Fuente et al. (2014), [(d)] Beuther et al. (2009), [(e)] Pagani et al. (2017), Beuther et al. (2009), [(f)] Belloche et al. (2013).

Table 9. COM abundances with respect to methyl formate.

Molecule	$X_{\rm methylformate}$							
	LM			IM		HM		
	IRAS4A2[a]	IRAS16293B[b]	IRAS2A[a]	Cep E-A	NGC 7129[c]	G29.96[d]	Orion KL[e]	SgrB2(N1)[f]
CH_3OH	39	51	63	46	50	5.2	21	41
H_2CO	0.7	5	5.7	3.4	1.0	–	–	1.1
H_2CCO	0.084	–	8.8(−2)	3.1(−1)	–	–	2.1(−3)	1.4
HCOOH	0.13–0.24	–	–	3.2(−2)	1.5	–	3.0(−2)	3.5(−2)
CH_3CHO	0.29–0.54	1.8(−1)	–	4.2(−1)	1.0(−1)	–	3.0(−3)	3.2(−1)
CH_3OCH_3	0.9	–	6.3(−1)	1.4	5.0(−1)	2.5	5.9(−1)	4.4
CH_3COCH_3	–	4.0(−2)	–	(1.0–3.2)(−1)	2.5(−2)	–	–	3.5(−1)
HNCO	0.066–0.11	7.5(−2)	–	6.1(−2)	4.0(−2)	–	4.3(−1)	2.9
NH_2CHO	0.028–0.057	2.5(−2)	1.5(−1)	1.7(−2)	–	–	4.3(−2)	2.9
CH_3CN	0.54–1.4	1.0(−1)	2.5(−1)	1.3(−1)	3.0(−1)	1.3(−1)	1.9(−1)	4.4
C_2H_5CN	4.1(−2)	1.0(−2)	1.9(−2)	(1.7–4.2)(−2)	7.0(−2)	1.3(−1)	3.0(−1)	4.1

Notes. Sources are ordered from left to right by increasing luminosity. [(a)] López-Sepulcre et al. (2017), Taquet et al. (2015), [(b)] Jørgensen et al. (2016), Coutens et al. (2016), Lykke et al. (2017), Calcutt et al. (2018), [(c)] Fuente et al. (2014), [(d)] Beuther et al. (2009), [(e)] Pagani et al. (2017), Beuther et al. (2009), [(f)] Belloche et al. (2013).

vides evidence for a different chemical composition in COMs. Recently, very sensitive observations of Cep E-mm have been obtained as part of the NOEMA Large Program "Seeds Of Life In Space" (SOLIS; Ceccarelli et al. 2017) and confirm the chemical differentiation observed between protostars Cep E-A and B (Lefloch in prep.).

Such a chemical differentiation has been reported in other multiple systems, like the low-mass protostars IRAS16293-2422 (2004a; 2016; 2011) and IRAS4A (Santangelo et al. 2015; López-Sepulcre et al. 2017), and, recently, towards the intermediate-mass protostars NGC 2264 CMM3 (Watanabe et al. 2017). With four examples at hand, we speculate that it could be a general feature of multiple protostellar systems and not a "pathological anomaly". There is no systematic trend between the millimetre thermal dust and molecular line emissions. Towards IRAS16293-2422 and IRAS4A, a rich content in COMs is observed towards the source with the less massive continuum source. Towards NGC 2264 CMM3, it is the most massive continuum component that displays a rich molecular content. The case of Cep E-mm appears similar to the latter one. High-mass star forming regions (HMSFRs) also present a rich chemical diversity. One of the best known examples is provided by Orion-KL. This source harbours: (i) a dichotomy between the spatial distribution of complex O-bearing and complex N-bearing species, with the latter species probing the hotter gas (see, e.g. Guélin et al. 2008; Favre et al. 2011; Friedel & Widicus Weaver 2012; Peng et al. 2013; Brouillet et al. 2013; Crockett et al. 2014, 2015) but also (ii) differences between supposed chemically related species (see, e.g. Favre et al. 2017; Pagani et al. 2017). Other examples are provided by W3(OH) (Qin et al. 2015; Nishimura et al. 2017) and SgrB2 (Belloche et al. 2008, 2013). In an observational study of four HMSFRs (Orion KL, G29.96, IRAS 23151+5912,

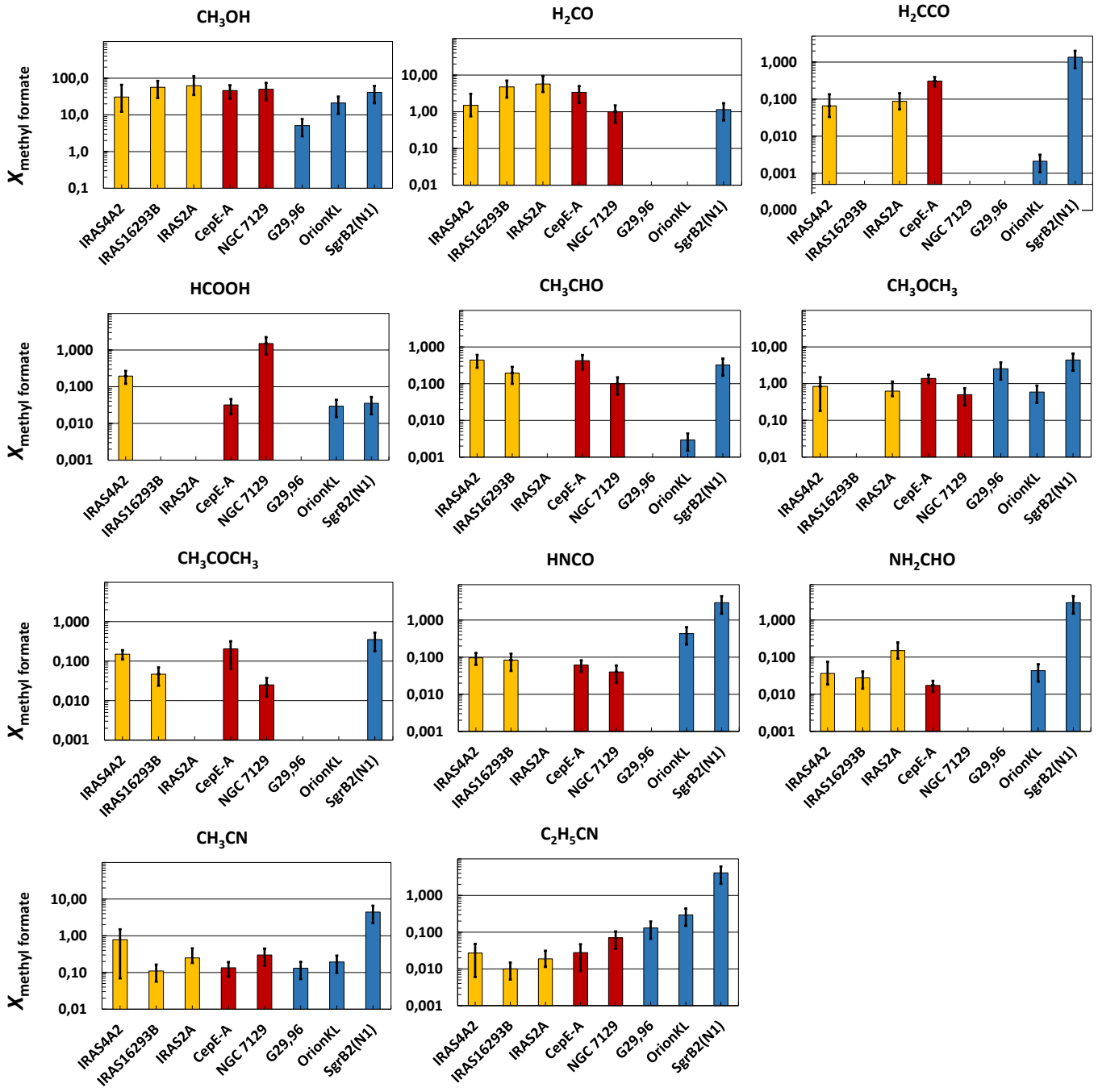

Fig. 10. Molecular abundances with respect to methyl formate towards low-mass hot corinos (yellow): IRAS2A (Taquet et al. 2015) and IRAS4A2 in NGC 1333 (Taquet et al. 2015; López-Sepulcre et al. 2017), IRAS16293B (Jørgensen et al. 2016; Coutens et al. 2016; Lykke et al. 2017; Calcutt et al. 2018); the intermediate-mass protostars (red): Cep E-A (this work) and NGC 7129 (Fuente et al. 2014); the high-mass hot cores (blue): G29.96 (Beuther et al. 2009), Orion KL (Pagani et al. 2017; Beuther et al. 2009) and SgrB2(N1) (Belloche et al. 2013). Sources are ordered from left to right by increasing luminosity.

and IRAS 05358+3543), Beuther et al. (2009) showed that the properties of CH_3OH can be easily accounted for by the physical conditions (temperature) in the cores, whereas the N-bearing species appear to be more selective as they are detected only towards the sources at the (evolved) hot core stage. Recently, in an ALMA study of the filamentary HMSFR G35.20, Sánchez-Monge et al. (2014) found that only three out of the six continuum cores of the filament display COM emission typical of hot cores. Several hypotheses have been proposed to account for the observed chemical differentiation. López-Sepulcre et al. (2017) proposed that the COM-rich protostar is either more massive and/or subject to a higher accretion rate, resulting in a lower envelope mass. Watanabe et al. (2017) suggest that the less massive protostar is related to a younger evolutionary stage in which the hot corino (hot core) is not yet developed, meaning that its dimensions are still very small. In Cep E-mm, the presence of high-velocity SiO jets provides evidence of active mass ejection around both protostars. The short dynamical timescales (500–1000 yr) also indicate that these ejections began recently, meaning that both sources are still in an early

evolutionary stage. Incidentally, Lykke et al. (2015) found an apparent correlation between the source luminosities and the relative abundance of complex organic molecules in a sample of sources including high-mass protostars. The authors have suggested that this could be the result of the timescale and the temperature experienced by a source during its evolution. The sample of sources with evidence for chemical differentiation should be increased in order to confirm this observational trend.

5.3. Comparison with hot cores and corinos

In this section, we compare the molecular abundances of COMs and chemically related species in Cep E-A with those obtained towards hot cores and corinos, relative to H_2 and methyl formate. The latter is commonly observed in star-forming regions and it does not suffer the drawbacks that affect methanol. Firstly, methanol line emission at low energy levels (E_{up} < 100 K) is often strongly contaminated by the outflow and the envelope, as shown in our single-dish analysis of CH_3OH emission (Sect. 4.2). Secondly, in the case of interferometric observations, the amount of filtered flux can vary significantly, thereby introducing biases in the derivation of molecular abundances. Finally, methyl formate likely suffers less from opacity issues in comparison to methanol. In order to minimise any possible bias in source comparison, we have selected targets in which the emission of hot cores and corinos could be isolated from the other components contributing to the emission (outflow, envelope). Also, the selected sources have been investigated in a systematic manner so that a large dataset is available: the IM protostar NGC 7129 (Fuente et al. 2014), the LM protostars IRAS2A (Taquet et al. 2015) and IRAS4A2 (López-Sepulcre et al. 2017; Taquet et al. 2015) in NGC 1333 and IRAS16293B (Jørgensen et al. 2016; Coutens et al. 2016; Lykke et al. 2017; Persson et al. 2018; Calcutt et al. 2018), and the hot cores G29.96 (Beuther et al. 2009), Orion KL (Beuther et al. 2009; Pagani et al. 2017) and SgrB2(N1) (Belloche et al. 2013). For all the sources but SgrB2(N1), we made use of interferometric observations. The molecular content of SgrB2(N1) was obtained by Belloche et al. (2013) from a careful multi-component analysis of a line survey with the IRAM 30 m telescope, which allowed them to disentangle the contributions of the two hot cores N1 and N2 of SgrB2(N). In the case of IRAS4A2, the molecular abundances of CH_3OH, H_2CO, and H_2CCO were taken from a previous study with the Plateau de Bure Interferometer by Taquet et al. (2015), as those species were not covered by the observations of López-Sepulcre et al. (2017). The angular resolution of their observations (2″) did not allow Taquet et al. (2015) to disentangle the contributions of protostars A1 and A2. They estimated the total gas column density from thermal dust continuum emission, which is dominated by the protostar A1, whereas the molecular emission arises mainly from the protostar A2. Therefore, the abundances of CH_3OH, H_2CO, and H_2CCO relative to H_2 as determined by Taquet et al. (2015), are underestimated. On the contrary, the molecular abundances relative to methyl formate are not affected by this bias. The physical properties of the parental cores (distance, luminosity, size) are summarised in Table 7.

The molecular abundances measured towards Cep E-A are summarised in Tables 8 and 9. In order to facilitate the readibility of Tables 8 and 9, we report only the molecular abundances. Abundance uncertainties are indicated by a thick black line in Fig. 10, which displays a graphical representation of the abundances of COMs with respect to methyl formate. We note that Fuente et al. (2014), Beuther et al. (2009) and Belloche et al. (2013) did not provide any uncertainty for molecular abundances in NGC 7129, Orion KL, G29.96 and SgrB2(N1). Beuther et al. (2009) pointed out that the uncertainties on the source temperature and sizes imply that the derived column densities must be taken with caution. Therefore, we have adopted a typical relative uncertainty of ∼35% for all column density determinations in these sources, similar to our own determinations in CepE-A, but we warn that they could be larger for the high-mass sources.

Overall, the molecular abundances derived in Cep E-A agree within a factor of four at most with those measured towards the IM protostar NGC 7129 by Fuente et al. (2005,2014). Most of the O- and N-bearing species of our study (CH_3CN, C_2H_5CN and HNCO) have very similar abundances. The only exceptions are CH_3COCH_3 and HCOOH. The CH_3COCH_3 abundance is higher towards Cep E-A by one order of magnitude. We note that this abundance determination also suffers from large uncertainties (see Sect. 4.4.2). On the contrary, HCOOH appears more abundant towards NGC 7129 by a factor 30.

Molecular abundances of the LM hot corinos IRAS2A and IRAS4A2 are also similar to those of Cep E-A. These conclusions are unchanged when comparing molecular abundances relative to methyl formate, as illustrated by the cases of H_2CO, $HCOOCH_3$ or CH_3OCH_3 (Fig. 10). Our results also agree with the tight correlation between CH_3OCH_3 and $HCOOCH_3$ previously reported by Jaber et al. (2014). The molecular abundances of O-bearing species are ≈1% of the CH_3OH abundance, whereas those of N-bearing species are lower by one order of magnitude, ∼0.1%.

The molecular abundances of O-bearing species appear rather similar towards LM and IM sources, independently of the luminosity. Towards HM sources, a large scatter is observed in the relative abundances of HCOOH and CH_3CHO. Comparison of molecular abundances relative to methyl formate does not reveal any specific trend as a function of the source luminosity for O-bearing species, from LM to HM. On the contrary, the abundances of N-bearing species display marked differences. As can be seen in Table 8, the abundances in G29.96, Orion KL, and Cep E-A are rather similar, whereas SgrB2(N) display higher abundances. Comparison of the molecular abundances relative to methyl formate reveals a trend, which is best illustrated by C_2H_5CN in Fig. 10, namely the relative molecular abundance increases with the source luminosity, from LM to HM. The same trend seems to be present in HNCO.

In summary, we find molecular abundances to be similar between Cep E-A , LM and IM hot corinos. The relative composition of O-bearing species with respect to methyl formate seems relatively independent of the source luminosity, contrary to C_2H_5CN, and perhaps other N-bearing species, which increases as a function of source luminosity.

6. Conclusions

We performed an unbiased spectral survey from 3 to 0.9 mm with the IRAM 30 m telescope. It was complemented with interferometric observations in the 3 and 1.3 mm bands with NOEMA at an angular resolution of 2.4 and 1.4″, respectively. We report bright emission of COMs and chemically related species towards the isolated IM protostellar core Cep E-mm. Our main conclusions are as follows.

Cep E-mm appears to be a protostellar binary system with components Cepe E-A and Cepe E-B separated by ≃1.7″(1250 au). Cep E-A dominates the bulk of the continuum emission and powers the long-studied high-velocity jet associated with HH377. Cep E-B powers another high-velocity

jet which propagates in a direction almost perpendicular to the Cep E-A jet.

We found evidence for a hot corino in a region of ≃0.7″ around Cep E-A. Cep E-B seems devoid of molecular emission at the sensitivity of our observations.

We successfully identified three components in the molecular spectral signatures: (a) an extremely broad line (eBL) component associated with the outflowing gas; (b) a narrow line (NL) component associated with the cold outer envelope of Cep E-mm; (c) a broad line (BL) component which traces the signature of the hot corino.

Methanol emission is dominated by the outflowing gas in transitions up to $E_{up} < 100$ K. At higher E_{up}, the hot corino dominates over the outflow.

Overall, COM molecular abundances in the Cep E-A hot corino are similar to those measured towards other low- and intermediate-mass protostars. N-bearing species are one order of magnitude less abundant that O-bearing species.

Relative to methyl formate, molecular abundances of O-bearing species are rather similar between protostars, independently of the source luminosity. On the contrary, a good correlation is observed between the relative C_2H_5CN abundance and the source luminosity.

Acknowledgements. J.O.Z., B.L. and C.F. thank Dr. Laurent Pagani for communication and discussions on Orion-KL. Based on observations carried out under project number W14AF with the IRAM NOEMA Interferometer. IRAM is supported by INSU/CNRS (France), MPG (Germany) and IGN (Spain). This work was supported by a grant from LabeX Osug@2020 (Investissements d'avenir – ANR10LABX56). C. Favre acknowledge the financial support for this work provided by the French space agency CNES along with the support from the Italian Ministry of Education, Universities and Research, project SIR (RBSI14ZRHR).

References

Alonso-Albi, T., Fuente, A., Crimier, N., et al. 2010, A&A, 518, A52
Ayala, S., Noriega-Crespo, A., Garnavich, P. M., et al. 2000, AJ, 120, 909
Belloche, A., Menten, K. M., Comito, C., et al. 2008, A&A, 482, 179
Belloche, A., Müller, H. S. P., Menten, K. M., & Schilke, P. 2013, A&A, 559, A47
Bottinelli, S., Ceccarelli, C., Neri, R., et al. 2004a, ApJ, 617, L69
Bottinelli, S., Ceccarelli, C., Lefloch, B., et al. 2004b, ApJ, 615, 354
Bottinelli, S., Ceccarelli, C., Williams, J. P., & Lefloch, B. 2007, A&A, 463, 601
Beuther, H., Zhang, Q., Bergin, E. A., et al. 2007, A&A, 468, 1045
Beuther, H., Zhang, Q., Bergin, E. A., & Sridharan, T. K. 2009, AJ, 137, 406
Bianchi, E., Codella, C., Ceccarelli, C., et al. 2017, MNRAS, 467, 3011
Brouillet, N., Despois, D., Baudry, A., et al. 2013, A&A, 550, A46
Calcutt, H., Jørgensen, J. K., & Müller, H. S. P. 2018, A&A, 616, A90
Caselli, P., & Ceccarelli, C. 2012, A&ARv, 20, 56
Cazaux, S., Tielens, A. G. G. M., Ceccarelli, C., et al. 2003, ApJ, 593, L51
Ceccarelli, C., Caselli, P., Herbst, E., Tielens, A. G. G. M., & Caux, E. 2007, Protostars and Planets V, 47
Ceccarelli, C., Bacmann, A., Boogert, A., et al. 2010, A&A, 521, L22
Ceccarelli, C., Caselli, P., Fontani, F., et al. 2017, ApJ, 850, 176
Codella, C., Ceccarelli, C., Cabrit, S., et al. 2016, A&A, 586, L3
Coutens, A., Jørgensen, J. K., van der Wiel, M. H. D., et al. 2016, A&A, 590, L6
Crimier, N., Ceccarelli, C., Alonso-Albi, T., et al. 2010, A&A, 516, A102
Crockett, N. R., Bergin, E. A., Neill, J. L., et al. 2014, ApJ, 787, 112
Crockett, N. R., Bergin, E. A., Neill, J. L., et al. 2015, ApJ, 806, 239
Favre, C., Despois, D., Brouillet, N., et al. 2011, A&A, 532, A32
Favre, C., Pagani, L., Goldsmith, P. F., et al. 2017, A&A, 604, L2
Friedel, D. N., & Widicus Weaver, S. L. 2012, ApJS, 201, 17
Fuente, A., Neri, R., & Caselli, P. 2005, A&A, 444, 481
Fuente, A., Ceccarelli, C., Neri, R., et al. 2007, A&A, 468, L37
Fuente, A., Cernicharo, J., Caselli, P., et al. 2014, A&A, 568, A65
Goldsmith, P. F., & Langer, W. D. 1999, ApJ, 517, 209
Guélin, M., Brouillet, N., Cernicharo, J., Combes, F., & Wootten, A. 2008, Ap&SS, 313, 45
Higuchi, A. E., Sakai, N., Watanabe, Y., et al. 2018, ApJS, 236, 52
Hogerheijde, M. R., van Dishoeck, E. F., Salverda, J. M., & Blake, G. A. 1999, ApJ, 513, 350
Imai, M., Sakai, N., Oya, Y., et al. 2016, ApJ, 830, L37
Jaber, A. A., Ceccarelli, C., Kahane, C., & Caux, E. 2014, ApJ, 791, 29
Jørgensen, J. K., Bourke, T. L., Nguyen Luong, Q., & Takakuwa, S. 2011, A&A, 534, A100
Jørgensen, J. K., van der Wiel, M. H. D., Coutens, A., et al. 2016, A&A, 595, A117
Kama, M., Dominik, C., Maret, S., et al. 2010, A&A, 521, L39
Langer, W. D. 1992, IAU Symp., 150, 193
Lefloch, B., Eisloeffel, J., & Lazareff, B. 1996, A&A, 313, L17
Lefloch, B., Castets, A., Cernicharo, J., & Loinard, L. 1998, ApJ, 504, L109
Lefloch, B., Cernicharo, J., Pacheco, S., & Ceccarelli, C. 2011, A&A, 527, L3
Lefloch, B., Gusdorf, A., Codella, C., et al. 2015, A&A, 581, A4
Lefloch, B., Ceccarelli, C., Codella, C., et al. 2017, MNRAS, 469, L73
Lefloch, B., Bachiller, R., Ceccarelli, C., et al. 2018, MNRAS, 477, 4792
Leurini, S., Codella, C., Cabrit, S., et al. 2016, A&A, 595, L4
López-Sepulcre, A., Taquet, V., Sánchez-Monge, Á., et al. 2013, A&A, 556, A62
López-Sepulcre, A., Jaber, A. A., Mendoza, E., et al. 2015, MNRAS, 449, 2438
López-Sepulcre, A., Sakai, N., Neri, R., et al. 2017, A&A, 606, A121
Lykke, J. M., Favre, C., Bergin, E. A., & Jørgensen, J. K. 2015, A&A, 582, A64
Lykke, J. M., Coutens, A., Jørgensen, J. K., et al. 2017, A&A, 597, A53
Maret, S., Hily-Blant, P., Pety, J., Bardeau, S., & Reynier, E. 2011, A&A, 526, A47
Moro-Martín, A., Noriega-Crespo, A., Molinari, S., et al. 2001, ApJ, 555, 146
Müller, H. S. P., Schlöder, F., Stutzki, J., & Winnewisser, G. 2005, J. Mol. Struct., 742, 215
Neri, R., Fuente, A., Ceccarelli, C., et al. 2007, A&A, 468, L33
Nishimura, Y., Watanabe, Y., Harada, N., et al. 2017, ApJ, 848, 17
Öberg, K. I., van der Marel, N., Kristensen, L. E., & van Dishoeck, E. F. 2011, ApJ, 740, 14
Ossenkopf, V., & Henning, T. 1994, A&A, 291, 943
Oya, Y., Sakai, N., Watanabe, Y., et al. 2017, ApJ, 837, 174
Pagani, L., Favre, C., Goldsmith, P. F., et al. 2017, A&A, 604, A32
Palla, F., Cesaroni, R., Brand, J., et al. 1993, A&A, 280, 599
Peng, T. C., Despois, D., Brouillet, N., et al. 2013, A&A, 554, A78
Persson, M. V., Jørgensen, J. K., Müller, H. S. P., et al. 2018, A&A, 610, A54
Pickett, H. M., Poynter, R. L., & Cohen, E. A. 1998, J. Quant. Spectr. Rad. Transf., 60, 883
Pilbratt, G. L., Riedinger, J. R., Passvogel, T., et al. 2010, A&A, 518, L1
Qin, S.-L., Schilke, P., Wu, J., et al. 2015, ApJ, 803, 39
Sakai, N., Sakai, T., & Yamamoto, S. 2008, Ap&SS, 313, 153
Sánchez-Monge, Á., Beltrán, M. T., Cesaroni, R., et al. 2014, A&A, 569, A11
Santangelo, G., Codella, C., Cabrit, S., et al. 2015, A&A, 584, A126
Sargent, A. I. 1977, ApJ, 218, 736
Schreyer, K., Henning, T., van der Tak, F. F. S., Boonman, A. M. S., & van Dishoeck, E. F. 2002, A&A, 394, 561
Shimajiri, Y., Takahashi, S., Takakuwa, S., Saito, M., & Kawabe, R. 2008, ApJ, 683, 255
Taquet, V., López-Sepulcre, A., Ceccarelli, C., et al. 2015, ApJ, 804, 81
Watanabe, Y., Sakai, N., López-Sepulcre, A., et al. 2017, ApJ, 847, 108
Wouterloot, J. G. A., & Walmsley, C. M. 1986, A&A, 168, 237

Appendix A: Spectral properties of detected COM emission lines.

Table A.1. E-CH3OH emission lines from the hot corino detected with the IRAM 30 m telescope.

Species	Frequency (MHz)	Quantum numbers	E_{up} (K)	A_{ul} (10^{-5} s^{-1})	Flux (mK km s^{-1})	V_{lsr} (km s^{-1})	ΔV (km s^{-1})	T_{peak} (mK)
E-CH_3OH	84521.172	$5_{-1,0}$–$4_{0,0}$	32.5	0.2	1091 (21)	–12.7 (0.0)	5.2 (0.1)	198 (3)
	108893.945	$0_{0,0}$–$1_{-1,0}$	5.2	1.5	160 (18)	–11.9 (0.1)	4.3 (0.3)	35 (3)
	132890.759	$6_{-1,0}$–$5_{0,0}$	46.4	0.8	1178 (44)	–12.5 (0.0)	5.3 (0.1)	208 (6)
	145097.435	$3_{-1,0}$–$2_{-1,0}$	11.6	1.1	3854 (210)	–12.3 (0.1)	7.4 (0.4)	486 (12)
	145126.386	$3_{-2,0}$–$2_{-2,0}$	31.9	0.7	96 (35)	–12.2 (0.5)	4.5 (0.8)	20 (6)
	145131.864	$3_{1,0}$–$2_{1,0}$	27.1	1.1	562 (33)	–12.3 (0.1)	6.1 (0.2)	87 (4)
	145766.227	$16_{0,0}$–$16_{-1,0}$	319.7	0.8	41 (8)	–10.0 (0.4)	6.4 (1.0)	6 (1)
	150141.672	$14_{0,0}$–$14_{-1,0}$	248.2	1.0	38 (10)	–10.7 (0.4)	4.2 (0.9)	9 (2)
	153281.282	$12_{0,0}$–$12_{-1,0}$	185.9	1.3	43 (8)	–10.4 (0.2)	2.9 (0.5)	14 (2)
	154425.832	$11_{0,0}$–$11_{-1,0}$	158.2	1.4	80 (9)	–10.6 (0.1)	4.5 (0.4)	17 (1)
	155320.895	$10_{0,0}$–$10_{-1,0}$	132.7	1.5	83 (12)	–10.7 (0.2)	5.4 (0.7)	14 (1)
	155997.524	$9_{0,0}$–$9_{-1,0}$	109.6	1.7	138 (8)	–10.9 (0.1)	5.2 (0.2)	25 (1)
	156488.902	$8_{0,0}$–$8_{-1,0}$	88.7	1.8	102 (31)	–10.7 (0.1)	3.5 (0.6)	27 (7)
	156828.517	$7_{0,0}$–$7_{-1,0}$	70.2	1.9	139 (9)	–10.9 (0.0)	3.4 (0.2)	38 (2)
	157048.617	$6_{0,0}$–$6_{-1,0}$	54.0	2.0	147 (15)	–10.9 (0.1)	3.1 (0.2)	44 (4)
	157178.987	$5_{0,0}$–$5_{-1,0}$	40.0	2.0	160 (88)	–11.1 (0.2)	5.1 (1.7)	29 (13)
	157246.062	$4_{0,0}$–$4_{-1,0}$	28.4	2.1	181 (12)	–10.9 (0.0)	2.9 (0.1)	59 (3)
	165050.175	$1_{1,0}$–$1_{0,0}$	15.5	2.3	533 (24)	–12.0 (0.1)	6.9 (0.2)	72 (2)
	165061.130	$2_{1,0}$–$2_{0,0}$	20.1	2.3	219 (34)	–11.5 (0.1)	3.3 (0.4)	62 (7)
	165099.240	$3_{1,0}$–$3_{0,0}$	27.1	2.3	269 (63)	–11.5 (0.1)	4.0 (0.6)	64 (11)
	165190.475	$4_{1,0}$–$4_{0,0}$	36.4	2.3	201 (45)	–11.3 (0.1)	3.3 (0.5)	57 (9)
	165369.341	$5_{1,0}$–$5_{0,0}$	48.0	2.3	251 (37)	–11.2 (0.1)	3.6 (0.4)	66 (7)
	166169.098	$7_{1,0}$–$7_{0,0}$	78.2	2.3	190 (48)	–11.3 (0.2)	6.4 (0.8)	28 (6)
	166898.566	$8_{1,0}$–$8_{0,0}$	96.7	2.3	202 (12)	–11.0 (0.1)	4.5 (0.2)	42 (2)
	167931.056	$9_{1,0}$–$9_{0,0}$	117.6	2.3	150 (13)	–10.4 (0.1)	4.3 (0.3)	33 (2)
	168577.831	$4_{1,0}$–$3_{2,0}$	36.4	0.4	117 (47)	–11.6 (0.6)	8.6 (1.8)	13 (4)
	170060.592	$3_{2,0}$–$2_{1,0}$	28.3	2.5	1433 (35)	–11.9 (0.0)	6.9 (0.1)	195 (4)
	213427.061	$1_{1,0}$–$0_{0,0}$	15.5	3.4	286 (34)	–11.5 (0.3)	7.0 (0.6)	38 (3)
	217886.504	$20_{1,0}$–$20_{0,0}$	500.5	3.4	98 (48)	–11.0 (0.9)	5.9 (2.2)	16 (5)
	218440.063	$4_{2,0}$–$3_{1,0}$	37.6	4.7	688 (484)	–10.7 (0.6)	6.1 (1.1)	106 (72)
	229758.756	$8_{-1,0}$–$7_{0,0}$	81.2	4.2	509 (56)	–11.2 (0.1)	5.6 (0.4)	86 (7)
	232945.797	$10_{-3,0}$–$11_{-2,0}$	182.5	2.1	76 (38)	–10.2 (1.2)	8.0 (3.2)	9 (3)
	240241.490	$5_{3,0}$–$6_{2,0}$	74.6	1.4	54 (47)	–10.9 (1.0)	5.1 (2.7)	10 (7)
	241179.886	$5_{-3,1}$–$4_{-3,1}$	349.5	3.8	67 (28)	–11.0 (0.7)	5.9 (1.9)	11 (3)
	241700.159	$5_{0,0}$–$4_{0,0}$	40.0	6.0	828 (51)	–11.2 (0.1)	6.5 (0.3)	119 (5)
	241767.234	$5_{-1,0}$–$4_{-1,0}$	32.5	5.8	1677 (98)	–11.2 (0.1)	6.2 (0.2)	252 (12)
	241843.604	$5_{3,0}$–$4_{3,0}$	74.6	3.9	229 (13)	–9.5 (0.1)	6.3 (0.3)	34 (1)
	241852.299	$5_{-3,0}$–$4_{-3,0}$	89.6	3.9	147 (40)	–12.4 (0.6)	7.9 (1.7)	18 (3)
	241879.025	$5_{1,0}$–$4_{1,0}$	48.0	6.0	461 (46)	–11.1 (0.3)	6.1 (0.5)	71 (4)
	241904.147	$5_{-2,0}$–$4_{-2,0}$	52.8	5.1	619 (193)	–11.5 (0.2)	5.8 (0.8)	101 (28)
	241904.643	$5_{2,0}$–$4_{2,0}$	49.2	5.0	653 (151)	–10.9 (0.2)	5.9 (0.7)	105 (21)
	242446.084	$14_{-1,0}$–$13_{-2,0}$	241.0	2.3	53 (28)	–9.4 (0.9)	5.4 (2.3)	9 (3)
	254015.377	$2_{0,0}$–$1_{-1,0}$	12.2	1.9	566 (37)	–12.2 (0.2)	7.9 (0.4)	67 (3)
	261704.409	$12_{6,0}$–$13_{5,0}$	351.9	1.8	45 (41)	–10.4 (0.6)	3.5 (2.9)	12 (5)
	261805.675	$2_{1,0}$–$1_{0,0}$	20.1	5.6	436 (39)	–11.6 (0.2)	6.3 (0.4)	65 (4)
	265289.562	$6_{1,0}$–$5_{2,0}$	61.9	2.6	141 (21)	–11.1 (0.3)	5.8 (0.7)	23 (2)
	266838.148	$5_{2,0}$–$4_{1,0}$	49.2	7.7	569 (98)	–11.3 (0.1)	5.0 (0.4)	107 (16)
	267403.471	$9_{0,0}$–$8_{1,0}$	109.6	4.7	115 (1500)	–10.5 (4.6)	5.1 (22.3)	21 (263)
	268743.954	$9_{-5,0}$–$10_{-4,0}$	220.5	1.8	35 (19)	–11.7 (0.8)	3.9 (1.6)	8 (3)
	278304.512	$9_{-1,0}$–$8_{0,0}$	102.1	7.7	366 (66)	–11.7 (0.2)	4.7 (0.6)	73 (9)
	278599.037	$14_{4,0}$–$15_{3,0}$	331.8	3.6	89 (30)	–12.8 (0.8)	7.2 (1.9)	12 (2)
	337135.853	$3_{3,0}$–$4_{2,0}$	53.7	1.6	85 (96)	–11.1 (3.2)	5.2 (5.5)	16 (5)
	337642.478	$7_{1,1}$–$6_{1,1}$	348.4	16.5	79 (31)	–12.0 (0.6)	4.8 (1.5)	15 (4)
	337643.915	$7_{0,1}$–$6_{0,1}$	357.5	16.9	84 (29)	–10.7 (0.6)	5.0 (1.3)	16 (4)
	338124.488	$7_{0,0}$–$6_{0,0}$	70.2	16.9	532 (44)	–11.5 (0.1)	5.0 (0.3)	100 (5)
	338344.588	$7_{-1,0}$–$6_{-1,0}$	62.7	16.6	769 (68)	–11.4 (0.1)	3.9 (0.2)	187 (12)
	338559.963	$7_{-3,0}$–$6_{-3,0}$	119.8	14.0	128 (40)	–10.6 (0.5)	5.3 (1.3)	23 (5)
	338614.936	$7_{1,0}$–$6_{1,0}$	78.2	17.1	382 (42)	–11.1 (0.2)	5.4 (0.4)	66 (5)
	338721.693	$7_{2,0}$–$6_{2,0}$	79.4	15.5	311 (129)	–11.4 (0.2)	3.6 (0.8)	81 (29)
	338722.898	$7_{-2,0}$–$6_{-2,0}$	83.0	15.7	300 (178)	–10.4 (0.3)	3.6 (1.0)	78 (41)

Notes. Intensities are expressed in units of T_A^*.

Table A.2. A-CH3OH emission lines from the hot corino detected with the IRAM 30 m telescope.

Species	Frequency (MHz)	Quantum numbers	E_{up} (K)	A_{ul} (10^{-5} s^{-1})	Flux (mK km s^{-1})	V_{lsr} (km s^{-1})	ΔV (km s^{-1})	T_{peak} (mK)
A-CH_3OH	95169.391	$8_{0,+,0}$–$7_{1,+,0}$	83.5	0.2	618 (22)	–12.4 (0.0)	4.5 (0.1)	129 (3)
	95914.310	$2_{1,+,0}$–$1_{1,+,0}$	21.4	0.2	213 (23)	–13.1 (0.3)	7.0 (0.4)	28 (3)
	96741.371	$2_{0,+,0}$–$1_{0,+,0}$	7.0	0.3	1231 (85)	–12.5 (0.2)	5.2 (0.3)	223 (9)
	97582.798	$2_{1,-,0}$–$1_{1,-,0}$	21.6	0.3	201 (22)	–12.1 (0.1)	5.7 (0.4)	33 (3)
	132621.824	$6_{2,-,0}$–$7_{1,-,0}$	86.5	0.4	46 (8)	–10.3 (0.2)	4.0 (0.6)	11 (1)
	143865.795	$3_{1,+,0}$–$2_{1,+,0}$	28.3	1.1	310 (36)	–11.8 (0.1)	6.0 (0.5)	48 (4)
	145103.185	$3_{0,+,0}$–$2_{0,+,0}$	13.9	1.2	989 (89)	–12.7 (0.1)	4.3 (0.2)	216 (16)
	146368.328	$3_{1,-,0}$–$2_{1,-,0}$	28.6	1.1	494 (25)	–12.0 (0.1)	5.6 (0.2)	83 (3)
	156127.544	$6_{2,+,0}$–$7_{1,+,0}$	86.5	0.7	51 (7)	–10.3 (0.1)	3.5 (0.4)	14 (1)
	156602.395	$2_{1,+,0}$–$3_{0,+,0}$	21.4	0.9	210 (11)	–10.8 (0.1)	5.4 (0.2)	36 (1)
	201445.493	$5_{2,+,0}$–$6_{1,+,0}$	72.5	1.3	132 (52)	–9.5 (0.9)	6.8 (2.0)	18 (5)
	205791.270	$1_{1,+,0}$–$2_{0,+,0}$	16.8	6.3	231 (33)	–11.0 (0.3)	6.9 (0.8)	31 (3)
	231281.110	$10_{2,-,0}$–$9_{3,-,0}$	165.3	1.8	79 (34)	–10.7 (0.6)	4.6 (1.5)	16 (4)
	232418.521	$10_{2,+,0}$–$9_{3,+,0}$	165.4	1.9	81 (34)	–12.2 (0.9)	6.9 (2.2)	11 (3)
	234683.370	$4_{2,-,0}$–$5_{1,-,0}$	60.9	1.8	100 (30)	–11.9 (0.6)	6.3 (1.4)	15 (3)
	239746.219	$5_{1,+,0}$–$4_{1,+,0}$	49.1	5.7	489 (29)	–11.0 (0.1)	6.8 (0.3)	68 (3)
	241791.352	$5_{0,+,0}$–$4_{0,+,0}$	34.8	6.0	2353 (117)	–11.4 (0.0)	6.5 (0.2)	340 (14)
	241832.718	$5_{3,+,0}$–$4_{3,+,0}$	84.6	3.9	296 (40)	–11.0 (0.3)	6.5 (0.7)	43 (4)
	241833.106	$5_{3,-,0}$–$4_{3,-,0}$	84.6	3.9	301 (38)	–10.5 (0.2)	6.5 (0.7)	43 (3)
	241842.284	$5_{2,-,0}$–$4_{2,-,0}$	72.5	5.1	228 (3)	–11.2 (0.0)	6.4 (0.1)	33 (0)
	243915.788	$5_{1,-,0}$–$4_{1,-,0}$	49.7	6.0	336 (119)	–11.0 (0.3)	5.6 (1.1)	56 (16)
	247228.587	$4_{2,+,0}$–$5_{1,+,0}$	60.9	2.2	68 (31)	–10.6 (0.8)	5.4 (1.9)	12 (3)
	249887.467	$14_{3,-,0}$–$14_{2,+,0}$	293.5	8.2	70 (28)	–9.4 (0.7)	5.8 (1.7)	11 (3)
	250291.181	$13_{3,-,0}$–$13_{2,+,0}$	261.0	8.2	57 (20)	–11.9 (0.7)	5.9 (1.6)	9 (2)
	250506.853	$11_{0,+,0}$–$10_{1,+,0}$	153.1	4.2	255 (13)	–10.7 (0.1)	6.6 (0.3)	36 (1)
	250635.200	$12_{3,-,0}$–$12_{2,+,0}$	230.8	8.2	71 (21)	–11.8 (0.6)	6.0 (1.4)	11 (2)
	250924.398	$11_{3,-,0}$–$11_{2,+,0}$	203.0	8.2	65 (25)	–10.7 (0.6)	4.9 (1.4)	13 (3)
	251359.888	$9_{3,-,0}$–$9_{2,+,0}$	154.3	8.1	105 (24)	–11.0 (0.4)	5.8 (1.0)	17 (3)
	251517.309	$8_{3,-,0}$–$8_{2,+,0}$	133.4	7.9	132 (39)	–10.3 (0.7)	7.4 (1.9)	17 (2)
	251641.787	$7_{3,-,0}$–$7_{2,+,0}$	114.8	7.7	115 (19)	–10.3 (0.3)	5.4 (0.7)	20 (2)
	251738.437	$6_{3,-,0}$–$6_{2,+,0}$	98.5	7.4	152 (21)	–10.4 (0.2)	5.2 (0.6)	27 (2)
	251984.837	$8_{3,+,0}$–$8_{2,-,0}$	133.4	8.0	133 (21)	–10.6 (0.3)	5.4 (0.7)	23 (2)
	252090.409	$9_{3,+,0}$–$9_{2,-,0}$	154.2	8.1	116 (21)	–10.2 (0.3)	5.3 (0.7)	21 (2)
	252252.849	$10_{3,+,0}$–$10_{2,-,0}$	177.5	8.3	104 (19)	–11.0 (0.3)	4.8 (0.7)	20 (3)
	252485.675	$11_{3,+,0}$–$11_{2,-,0}$	203.0	8.4	91 (26)	–10.4 (0.5)	5.7 (1.2)	15 (3)
	253221.376	$13_{3,+,0}$–$13_{2,-,0}$	261.0	8.5	66 (22)	–10.7 (0.5)	4.6 (1.1)	14 (3)
	256228.714	$17_{3,+,0}$–$17_{2,-,0}$	404.8	9.0	65 (53)	–10.1 (1.4)	5.6 (4.0)	11 (4)
	257402.086	$18_{3,+,0}$–$18_{2,-,0}$	446.5	9.1	57 (25)	–11.5 (0.7)	4.4 (1.5)	12 (4)
	279351.887	$11_{2,-,0}$–$10_{3,-,0}$	190.9	3.5	42 (22)	–10.0 (0.6)	4.0 (1.6)	10 (3)
	281000.109	$11_{2,+,0}$–$10_{3,+,0}$	190.9	3.5	101 (24)	–11.1 (0.3)	4.4 (0.8)	22 (3)
	292672.889	$6_{1,-,0}$–$5_{1,-,0}$	63.7	10.6	530 (43)	–10.9 (0.1)	4.2 (0.3)	118 (6)
	302912.979	$12_{0,+,0}$–$11_{1,+,0}$	180.9	7.6	310 (36)	–10.6 (0.2)	4.9 (0.4)	59 (4)
	303366.921	$1_{1,-,0}$–$1_{0,+,0}$	16.9	22.6	829 (42)	–10.3 (0.1)	6.5 (0.2)	120 (4)
	304208.348	$2_{1,-,0}$–$2_{0,+,0}$	21.6	21.1	678 (55)	–10.5 (0.1)	4.9 (0.3)	130 (7)
	305473.491	$3_{1,-,0}$–$3_{0,+,0}$	28.6	16.3	645 (97)	–10.5 (0.1)	4.6 (0.4)	131 (16)
	307165.924	$4_{1,-,0}$–$4_{0,+,0}$	38.0	16.5	563 (60)	–10.4 (0.3)	6.0 (0.5)	88 (5)
	309290.360	$5_{1,-,0}$–$5_{0,+,0}$	49.7	16.8	285 (136)	–10.2 (0.3)	4.4 (1.0)	60 (25)
	331502.319	$11_{1,-,0}$–$11_{0,+,0}$	169.0	19.6	230 (48)	–10.6 (0.3)	4.1 (0.7)	53 (7)
	335582.017	$7_{1,+,0}$–$6_{1,+,0}$	79.0	16.3	293 (45)	–11.1 (0.2)	3.8 (0.5)	72 (7)
	336865.149	$12_{1,-,0}$–$12_{0,+,0}$	197.1	20.3	179 (46)	–11.3 (0.4)	5.4 (1.1)	31 (5)
	337297.484	$7_{1,+,1}$–$6_{1,+,1}$	390.0	16.5	80 (81)	–10.3 (1.6)	4.8 (4.2)	16 (7)
	338408.698	$7_{0,+,0}$–$6_{0,+,0}$	65.0	17.0	820 (73)	–11.5 (0.1)	3.8 (0.2)	200 (13)
	338486.322	$7_{5,+,0}$–$6_{5,+,0}$	202.9	8.4	98 (41)	–12.3 (0.7)	5.0 (1.6)	18 (5)
	338486.322	$7_{5,-,0}$–$6_{5,-,0}$	202.9	8.4	104 (43)	–12.4 (0.7)	5.5 (1.8)	18 (5)
	338512.632	$7_{4,-,0}$–$6_{4,-,0}$	145.3	11.5	185 (44)	–10.4 (0.3)	4.7 (0.9)	37 (5)
	338512.644	$7_{4,+,0}$–$6_{4,+,0}$	145.3	11.5	182 (44)	–10.4 (0.3)	4.6 (0.9)	37 (5)
	338512.853	$7_{2,-,0}$–$6_{2,-,0}$	102.7	15.7	180 (44)	–10.2 (0.3)	4.6 (0.9)	37 (5)
	338540.826	$7_{3,+,0}$–$6_{3,+,0}$	114.8	13.9	290 (42)	–11.7 (0.2)	5.4 (0.6)	50 (5)
	338543.152	$7_{3,-,0}$–$6_{3,-,0}$	114.8	13.9	293 (42)	–9.6 (0.2)	5.4 (0.6)	51 (5)
	338639.802	$7_{2,+,0}$–$6_{2,+,0}$	102.7	15.7	124 (40)	–11.0 (0.5)	4.8 (1.2)	24 (5)
	341415.615	$7_{1,-,0}$–$6_{1,-,0}$	80.1	17.1	180 (115)	–11.0 (0.3)	3.3 (1.1)	52 (28)
	342729.796	$13_{1,-,0}$–$13_{0,+,0}$	227.5	21.1	202 (83)	–10.6 (0.5)	4.8 (1.8)	40 (7)

Notes. Intensities are expressed in units of T_A^*.

Table A.3. Rare CH_3OH isotopologue emission lines from the hot corino detected with the IRAM 30 m telescope.

Species	Frequency (MHz)	Quantum numbers	E_{up} (K)	A_{ul} (10^{-5} s^{-1})	Flux (mK km s^{-1})	V_{lsr} (km s^{-1})	ΔV (km s^{-1})	T_{peak} (mK)
$^{13}CH_3OH$	141602.528	$3_{0,3,+}$–$2_{0,2,+}$	13.6	1.1	83 (17)	–11.7 (0.3)	5.9 (0.8)	13 (2)
	168676.499	$3_{2,1}$–$2_{1,1}$	35.9	2.5	46 (13)	–11.0 (0.3)	4.1 (1.0)	11 (2)
	235881.170	$5_{0,5}$–$4_{0,4}$	47.1	5.6	51 (28)	–9.3 (1.1)	6.2 (2.6)	8 (3)
	235938.220	$5_{-1,5}$–$4_{-1,4}$	39.6	5.4	89 (32)	–11.4 (1.0)	8.8 (2.4)	10 (2)
	236049.520	$5_{2,3,+}$–$4_{2,2,+}$	71.8	4.8	59 (24)	–10.4 (0.8)	5.7 (1.8)	10 (3)
	255214.891	$7_{3,5,+}$–$7_{2,6,-}$	113.5	8.1	38 (23)	–11.7 (0.7)	4.2 (2.0)	8 (3)
CH_2DOH	88073.074	$2_{1,2,0}$–$1_{1,1,0}$	10.4	0.1	13 (4)	–11.3 (0.2)	2.0 (0.5)	6 (1)
	91586.845	$4_{1,3,0}$–$4_{0,4,0}$	25.8	0.5	44 (8)	–11.2 (0.2)	3.7 (0.5)	11 (1)
	98031.213	$4_{0,4,0}$–$3_{1,3,0}$	21.4	0.2	33 (5)	–11.5 (0.1)	2.3 (0.3)	13 (1)
	132093.628	$3_{1,3,0}$–$2_{1,2,0}$	16.7	0.6	43 (6)	–10.9 (0.1)	2.6 (0.3)	15 (1)
	134065.381	$3_{0,3,0}$–$2_{0,2,0}$	12.9	0.7	72 (17)	–11.3 (0.3)	5.5 (1.0)	12 (2)
	136151.142	$3_{1,2,0}$–$2_{1,1,0}$	17.1	0.7	42 (19)	–10.2 (0.9)	5.5 (1.7)	7 (2)
	161602.516	$3_{1,3,1}$–$4_{0,4,0}$	29.2	0.9	52 (19)	–11.0 (0.5)	5.9 (2.0)	8 (1)
	172015.919	$2_{1,2,0}$–$1_{0,1,0}$	10.4	2.2	71 (21)	–10.9 (0.3)	3.8 (0.8)	17 (4)
	237249.907	$7_{2,5,0}$–$7_{1,6,0}$	76.4	8.1	32 (7)	–12.4 (0.4)	4.6 (0.8)	6 (1)
	240187.202	$6_{2,4,0}$–$6_{1,5,0}$	61.3	7.7	163 (17)	–10.3 (0.2)	6.1 (0.5)	25 (2)
	243225.990	$5_{2,3,0}$–$5_{1,4,0}$	48.4	6.7	89 (35)	–9.5 (0.7)	6.0 (1.9)	14 (3)
	253637.057	$4_{2,2,1}$–$3_{1,2,2}$	48.0	6.0	103 (46)	–10.2 (1.0)	7.2 (2.5)	13 (4)
	255647.816	$3_{2,2,0}$–$3_{1,3,0}$	29.0	6.3	154 (44)	–10.9 (0.6)	6.7 (1.4)	21 (4)
	256731.552	$4_{1,4,0}$–$3_{0,3,0}$	25.2	6.9	101 (46)	–11.2 (0.6)	4.4 (1.6)	22 (6)
	257895.673	$4_{2,3,1}$–$3_{1,3,2}$	48.0	6.3	89 (45)	–10.5 (0.7)	4.2 (1.6)	20 (7)
	264017.721	$6_{1,6,0}$–$5_{1,5,0}$	48.4	5.8	131 (31)	–9.9 (0.4)	5.3 (1.0)	23 (4)
	265509.198	$6_{1,6,2}$–$5_{1,5,2}$	67.5	7.5	70 (28)	–10.7 (0.6)	4.2 (1.3)	16 (4)
	267031.234	$6_{0,6,1}$–$5_{0,5,1}$	58.4	7.5	50 (19)	–10.3 (0.6)	4.7 (1.3)	10 (2)
	267634.613	$6_{0,6,0}$–$5_{0,5,0}$	45.0	6.3	155 (33)	–10.9 (0.3)	4.4 (0.7)	33 (5)
	268012.863	$6_{2,5,0}$–$5_{2,4,0}$	61.2	5.4	111 (16)	–10.7 (0.3)	6.9 (0.7)	15 (1)
	268059.704	$6_{2,4,1}$–$5_{2,3,1}$	71.6	7.1	71 (34)	–11.9 (0.8)	5.2 (2.0)	13 (4)
	269886.317	$6_{1,5,2}$–$5_{1,4,2}$	68.2	7.9	50 (23)	–10.2 (0.4)	3.7 (1.4)	12 (4)
	270299.931	$7_{2,6,0}$–$7_{1,7,0}$	76.2	8.8	102 (24)	–11.5 (0.4)	5.7 (1.0)	17 (3)
	270734.570	$6_{1,5,1}$–$5_{1,4,1}$	62.0	7.8	72 (27)	–11.3 (0.6)	4.5 (1.3)	15 (4)
	272098.060	$6_{1,5,0}$–$5_{1,4,0}$	49.8	6.4	96 (35)	–9.9 (0.6)	5.1 (1.4)	18 (4)
	275510.466	$8_{2,7,0}$–$8_{1,8,0}$	93.3	9.4	75 (17)	–11.9 (0.2)	3.7 (0.7)	19 (3)

Notes. Intensities are expressed in units of T_A^*.

Table A.4. COMs emission lines from the hot corino detected with the IRAM 30 m telescope.

Species	Frequency (MHz)	Quantum numbers	E_{up} (K)	A_{ul} (10^{-5} s^{-1})	Flux (mK km s^{-1})	V_{lsr} (km s^{-1})	ΔV (km s^{-1})	T_{peak} (mK)
CH_3OCH_3	132524.779	$8_{0,8,0}$–$7_{1,7,0}$	32.4	1.1	46 (12)	–11.6 (0.2)	2.4 (0.5)	18 (3)
	132525.239	$8_{0,8,1}$–$7_{1,7,1}$	32.4	1.1	43 (11)	–10.5 (0.2)	2.1 (0.4)	19 (3)
	222247.600	$4_{3,2,1}$–$3_{2,1,1}$	21.8	3.4	67 (33)	–11.5 (0.9)	5.9 (2.2)	11 (3)
	222247.600	$4_{3,2,3}$–$3_{2,1,3}$	21.8	4.9	68 (28)	–11.7 (0.7)	5.4 (1.7)	12 (3)
	222254.582	$4_{3,2,0}$–$3_{2,1,0}$	21.8	4.9	58 (35)	–12.3 (1.0)	5.5 (2.6)	10 (4)
	222426.698	$4_{3,1,3}$–$3_{2,2,3}$	21.8	4.9	43 (38)	–9.5 (2.0)	7.7 (5.7)	5 (3)
	223202.244	$8_{2,7,1}$–$7_{1,6,1}$	38.3	3.1	39 (37)	–9.1 (0.7)	4.0 (3.0)	9 (5)
	237618.803	$9_{2,8,2}$–$8_{1,7,2}$	46.5	3.8	75 (39)	–13.4 (1.1)	6.4 (2.6)	11 (4)
	237618.808	$9_{2,8,3}$–$8_{1,7,3}$	46.5	3.8	84 (58)	–13.5 (1.7)	7.4 (4.4)	11 (4)
	237620.887	$9_{2,8,1}$–$8_{1,7,1}$	46.5	3.8	81 (37)	–10.9 (1.0)	7.0 (2.4)	11 (3)
	237622.968	$9_{2,8,0}$–$8_{1,7,0}$	46.5	3.8	79 (39)	–8.0 (1.0)	6.5 (2.4)	11 (4)
	240989.939	$5_{3,3,0}$–$4_{2,2,0}$	26.3	5.4	55 (33)	–11.8 (1.0)	5.5 (2.4)	10 (4)
	258548.775	$14_{1,14,2}$–$13_{0,13,2}$	93.3	10.4	177 (53)	–11.3 (0.7)	7.5 (1.7)	22 (4)
	258548.775	$14_{1,14,3}$–$13_{0,13,3}$	93.3	10.4	175 (52)	–11.3 (0.7)	7.3 (1.6)	23 (4)
	258549.019	$14_{1,14,1}$–$13_{0,13,1}$	93.3	10.4	175 (51)	–10.9 (0.7)	7.1 (1.6)	23 (4)
	258549.263	$14_{1,14,0}$–$13_{0,13,0}$	93.3	10.4	180 (53)	–10.7 (0.7)	7.5 (1.7)	23 (4)
	269608.758	$15_{0,15,0}$–$14_{1,14,0}$	106.3	12.0	121 (38)	–9.3 (0.8)	8.7 (2.2)	13 (2)
	269608.775	$15_{0,15,1}$–$14_{1,14,1}$	106.3	12.0	106 (34)	–9.3 (0.8)	7.7 (1.9)	13 (3)
	269608.791	$15_{0,15,3}$–$14_{1,14,3}$	106.3	12.0	109 (37)	–9.4 (0.8)	7.7 (2.0)	13 (3)
	269608.792	$15_{0,15,2}$–$14_{1,14,2}$	106.3	12.0	118 (47)	–10.1 (1.1)	8.5 (2.8)	13 (3)
$HCOOCH_3$	89314.657	$8_{1,8,1}$–$7_{1,7,1}$	20.1	1.0	18 (12)	–11.4 (0.4)	2.9 (1.8)	6 (1)
	90227.659	$8_{0,8,2}$–$7_{0,7,2}$	20.1	1.1	9 (0)	–11.1 (0.0)	1.6 (0.0)	5 (0)
	90229.624	$8_{0,8,0}$–$7_{0,7,0}$	20.1	1.1	13 (5)	–11.9 (0.3)	2.1 (0.6)	6 (1)
	103466.572	$8_{2,6,2}$–$7_{2,5,2}$	24.6	1.5	17 (12)	–12.0 (0.8)	2.8 (1.8)	6 (1)
	103478.663	$8_{2,6,0}$–$7_{2,5,0}$	24.6	1.5	11 (5)	–10.4 (0.2)	1.8 (0.6)	5 (2)
	129296.357	$10_{2,8,2}$–$9_{2,7,2}$	36.4	3.1	26 (9)	–11.7 (0.2)	1.5 (0.4)	17 (4)
	132107.205	$12_{1,12,0}$–$11_{1,11,0}$	42.4	3.4	18 (5)	–11.1 (0.2)	1.8 (0.4)	10 (2)
	132246.730	$12_{0,12,0}$–$11_{0,11,0}$	42.4	3.4	30 (5)	–10.5 (0.1)	2.8 (0.4)	10 (1)
	132921.937	$11_{1,10,2}$–$10_{1,9,2}$	40.4	3.4	15 (14)	–11.0 (0.3)	0.9 (0.7)	16 (6)
	132928.736	$11_{1,10,0}$–$10_{1,9,0}$	40.4	3.4	22 (10)	–11.7 (0.3)	1.7 (0.6)	12 (4)
CH_3CN	110364.354	6_3–5_3	82.8	8.3	41 (19)	–11.4 (0.2)	3.0 (0.9)	13 (4)
	110374.989	6_2–5_2	47.1	9.9	42 (16)	–10.9 (0.2)	2.8 (0.7)	14 (4)
	128769.436	7_2–6_2	53.3	16.4	88 (22)	–11.1 (0.2)	2.8 (0.6)	29 (4)
	128779.364	7_0–6_0	24.7	17.8	293 (30)	–11.3 (0.2)	5.9 (0.5)	47 (3)
	147149.068	8_3–7_3	96.1	23.1	130 (7)	–11.2 (0.1)	4.9 (0.2)	25 (1)
	147163.244	8_2–7_2	60.4	25.2	56 (13)	–10.9 (0.1)	3.1 (0.5)	17 (3)
	202320.443	11_3–10_3	122.6	65.6	115 (41)	–10.5 (0.7)	5.9 (1.6)	18 (4)
	202339.922	11_2–10_2	86.9	68.6	95 (29)	–10.8 (0.6)	4.7 (1.1)	19 (4)
	202351.612	11_1–10_1	65.4	70.3	278 (49)	–15.6 (0.5)	9.4 (1.3)	28 (3)
	202355.509	11_0–10_0	58.3	70.9	280 (48)	–9.7 (0.5)	9.8 (1.3)	27 (3)
	220709.017	12_3–11_3	133.2	86.6	101 (25)	–10.3 (0.5)	6.1 (1.2)	16 (2)
	220743.011	12_1–11_1	76.0	91.8	208 (32)	–11.8 (0.5)	10.1 (1.2)	19 (2)
	220747.261	12_0–11_0	68.9	92.4	234 (33)	–5.5 (0.5)	11.7 (1.2)	19 (2)
	239096.497	13_3–12_3	144.6	111.5	76 (27)	–10.1 (0.5)	4.7 (1.3)	15 (3)
	239133.313	13_1–12_1	87.5	117.2	208 (41)	–12.3 (0.6)	10.1 (1.5)	19 (2)
	239137.916	13_0–12_0	80.3	117.9	213 (41)	–6.6 (0.6)	10.3 (1.6)	19 (2)
	257527.384	14_0–13_0	92.7	147.6	219 (54)	–9.5 (1.0)	12.7 (2.4)	16 (2)
	275910.263	15_1–14_1	113.1	181.1	151 (55)	–12.0 (1.1)	9.4 (2.7)	15 (3)
	294279.750	16_2–15_2	148.6	217.7	74 (28)	–10.5 (0.4)	3.5 (1.0)	20 (5)
	294296.728	16_1–15_1	127.2	220.4	186 (38)	–11.7 (0.5)	7.8 (1.2)	22 (3)

Notes. Intensities are expressed in units of T_A^*.

Table A.4. continued.

Species	Frequency (MHz)	Quantum numbers	E_{up} (K)	A_{ul} (10^{-5} s^{-1})	Flux (mK km s^{-1})	V_{lsr} (km s^{-1})	ΔV (km s^{-1})	T_{peak} (mK)
H_2CCO	140127.474	$7_{1,7}$–$6_{1,6}$	40.0	3.0	85 (21)	–11.1 (0.2)	5.4 (1.0)	15 (3)
	142768.945	$7_{1,6}$–$6_{1,5}$	40.5	3.1	112 (15)	–11.3 (0.2)	6.7 (0.6)	16 (2)
	161634.073	$8_{0,8}$–$7_{0,7}$	34.9	4.7	86 (45)	–11.4 (0.5)	6.1 (2.6)	13 (4)
	163160.881	$8_{1,7}$–$7_{1,6}$	48.3	4.7	133 (23)	–11.5 (0.2)	5.5 (0.6)	23 (3)
	203940.225	$10_{1,9}$–$9_{1,8}$	66.9	9.4	69 (20)	–10.6 (0.6)	4.5 (1.0)	14 (3)
	220177.569	$11_{1,11}$–$10_{1,10}$	76.5	11.9	41 (35)	–11.7 (1.2)	3.3 (2.2)	12 (6)
	224327.250	$11_{1,10}$–$10_{1,9}$	77.7	12.6	69 (21)	–10.8 (0.5)	4.5 (1.0)	15 (3)
	244712.269	$12_{1,11}$–$11_{1,10}$	89.4	16.4	50 (34)	–10.6 (0.6)	3.9 (2.1)	12 (5)
	265095.049	$13_{1,12}$–$12_{1,11}$	102.1	21.0	50 (27)	–11.1 (0.8)	5.2 (2.3)	9 (3)
$H_2^{13}CO$	137449.950	$2_{1,2}$–$1_{1,1}$	21.7	4.9	174 (31)	–11.9 (0.2)	6.3 (0.8)	26 (3)
	141983.740	$2_{0,2}$–$1_{0,1}$	10.2	7.2	150 (17)	–11.9 (0.2)	7.1 (0.5)	20 (2)
	146635.671	$2_{1,1}$–$1_{1,0}$	22.4	6.0	173 (31)	–11.8 (0.1)	5.9 (0.7)	27 (4)
	206131.626	$3_{1,3}$–$2_{1,2}$	31.6	21.1	892 (96)	–10.8 (0.2)	6.4 (0.6)	130 (9)
	212811.184	$3_{0,3}$–$2_{0,2}$	20.4	26.1	201 (43)	–12.4 (0.5)	7.5 (1.2)	25 (3)
	274762.112	$4_{1,4}$–$3_{1,3}$	44.8	54.7	259 (56)	–11.1 (0.5)	7.0 (1.3)	35 (4)
	293126.515	$4_{1,3}$–$3_{1,2}$	47.0	66.4	222 (46)	–9.8 (0.3)	4.9 (0.8)	42 (6)
	343325.713	$5_{1,5}$–$4_{1,4}$	61.3	111.8	290 (85)	–10.8 (0.4)	4.8 (1.1)	57 (10)

Table A.5. NOEMA Observations of Cep E-A.

Species	Frequency (MHz)	Quantum numbers	E_{up} (K)	A_{ul} (10^{-5} s^{-1})	Flux (mJ beam^{-1} km s^{-1})	V_{lsr} (km s^{-1})	ΔV (km s^{-1})	T_{peak} (mJ beam^{-1})
E-CH_3OH	216945.521	$5_{1,0}$–$4_{2,0}$	48.0	1.2	807 (37)	–10.3 (0.1)	5.2 (0.2)	145.9 (4.5)
	217886.504	$20_{1,0}$–$20_{0,0}$	500.5	3.4	380 (28)	–11.1 (0.1)	5.5 (0.3)	65.4 (3.1)
	218440.063	$4_{2,0}$–$3_{1,0}$	37.6	4.7	1330 (49)	–10.4 (0.0)	4.7 (0.1)	264.5 (6.1)
	220078.561	$8_{0,0}$–$7_{1,0}$	88.7	2.5	975 (47)	–10.5 (0.1)	6.3 (0.2)	146.3 (3.9)
A-CH_3OH	217299.205	$6_{1,-,1}$–$7_{2,-,1}$	373.9	4.3	504 (29)	–10.8 (0.1)	5.8 (0.3)	82.1 (3.1)
	217642.677	$15_{6,-,1}$–$16_{5,-,1}$	745.6	1.9	188 (26)	–12.3 (0.3)	5.5 (0.6)	32.4 (3.0)
	217642.678	$15_{6,+,1}$–$16_{5,+,1}$	745.6	1.9	179 (25)	–12.3 (0.2)	5.3 (0.5)	31.8 (2.9)
CH_2DOH	86668.751	$2_{1,1,0}$–$2_{0,2,0}$	10.6	0.5	127 (25)	–11.9 (0.9)	9.8 (1.4)	12.1 (1.6)
	218316.390	$5_{2,4,1}$–$5_{1,5,1}$	58.7	0.9	1602 (222)	–12.5 (0.3)	7.5 (0.9)	33.8 (2.6)
	219551.485	$5_{1,5,1}$–$4_{1,4,1}$	48.2	0.7	286 (29)	–10.0 (0.3)	7.9 (0.6)	33.8 (2.2)
	220071.805	$5_{1,5,0}$–$4_{1,4,0}$	35.8	3.3	1012 (106)	–10.4 (0.2)	6.6 (0.6)	56.8 (3.3)
H_2CCO	220177.569	$11_{1,11}$–$10_{1,10}$	76.5	11.9	323 (34)	–10.8 (0.2)	6.6 (0.5)	46.2 (3.1)
HCOOH	220038.072	$10_{0,10}$–$9_{0,9}$	58.6	11.5	117 (39)	–12.1 (0.8)	6.0 (1.9)	13.4 (4.0)
$HCOOCH_3$	216830.197	$18_{2,16,2}$–$17_{2,15,2}$	105.7	14.8	162 (11)	–10.6 (0.2)	8.4 (0.5)	18.2 (0.6)
	216838.889	$18_{2,16,0}$–$17_{2,15,0}$	105.7	14.8	114 (8)	–10.2 (0.1)	4.4 (0.3)	24.3 (1.1)
	216964.765	$20_{1,20,1}$–$19_{1,19,1}$	111.5	15.3	509 (13)	–12.6 (0.1)	7.6 (0.2)	62.8 (1.1)
	216965.900	$20_{1,20,0}$–$19_{1,19,0}$	111.5	15.3	504 (16)	–11.1 (0.1)	7.5 (0.2)	62.9 (1.3)
	216966.246	$20_{0,20,2}$–$19_{0,19,2}$	111.5	15.3	500 (49)	–10.6 (0.2)	7.5 (0.6)	62.3 (3.9)
	216967.420	$20_{0,20,0}$–$19_{0,19,0}$	111.5	15.3	514 (47)	–9.0 (0.2)	7.6 (0.5)	63.2 (3.7)
	218108.438	$17_{4,13,5}$–$16_{4,12,5}$	289.7	14.8	88 (35)	–10.9 (1.0)	7.9 (2.4)	10.5 (2.7)
	218280.900	$17_{3,14,2}$–$16_{3,13,2}$	99.7	15.1	147 (29)	–11.5 (0.3)	5.1 (0.8)	27.1 (3.5)
	218297.890	$17_{3,14,0}$–$16_{3,13,0}$	99.7	15.1	123 (30)	–11.7 (0.5)	5.6 (1.0)	20.8 (3.4)
	220166.888	$17_{4,13,2}$–$16_{4,12,2}$	103.2	15.2	152 (34)	–11.0 (0.5)	6.5 (1.1)	21.9 (3.2)
	220190.285	$17_{4,13,0}$–$16_{4,12,0}$	103.1	15.2	140 (49)	–11.9 (0.6)	6.8 (2.1)	19.3 (3.3)
CH_3CHO	219820.400	$4_{2,3,1}$–$3_{1,3,1}$	18.3	1.5	65 (11)	–10.8 (0.2)	4.5 (0.6)	13.6 (1.5)
CH_3OCH_3	217191.424	$22_{4,19,}$–$22_{3,20,}$	253.4	4.3	113 (24)	–11.8 (0.4)	5.4 (1.1)	54.0 (4.1)
CH_3COCH_3	218127.207	$20_{2,18,0}$–$19_{3,17,1}$	119.1	22.1	179 (25)	–11.7 (0.3)	6.1 (0.6)	27.4 (2.5)
HNCO	218890	$10_{1,10}$–$9_{1,9}$	101.1	14.6	437 (18)	*	6.7 (0.3)	56.4 (2.9)
	219734	$10_{2,9/8}$–$9_{2,8/7}$	231.1	14.3	283 (17)	*	9.4 (0.8)	35.3 (2.9)
	219798	$10_{0,10}$–$9_{0,9}$	58.0	15.0	398 (17)	*	5.7 (0.5)	86.3 (2.9)
NH_2CHO	218459.653	$10_{1,9}$–$9_{1,8}$	60.8	74.7	197 (59)	–12.1 (0.6)	6.8 (1.7)	27.1 (4.8)

Notes. (*) Unresolved multiplet lines.